Cell Reports

Article

The ARID1A-METTL3-m6A axis ensures effective RNase H1-mediated resolution of R-loops and genome stability

Graphical abstract

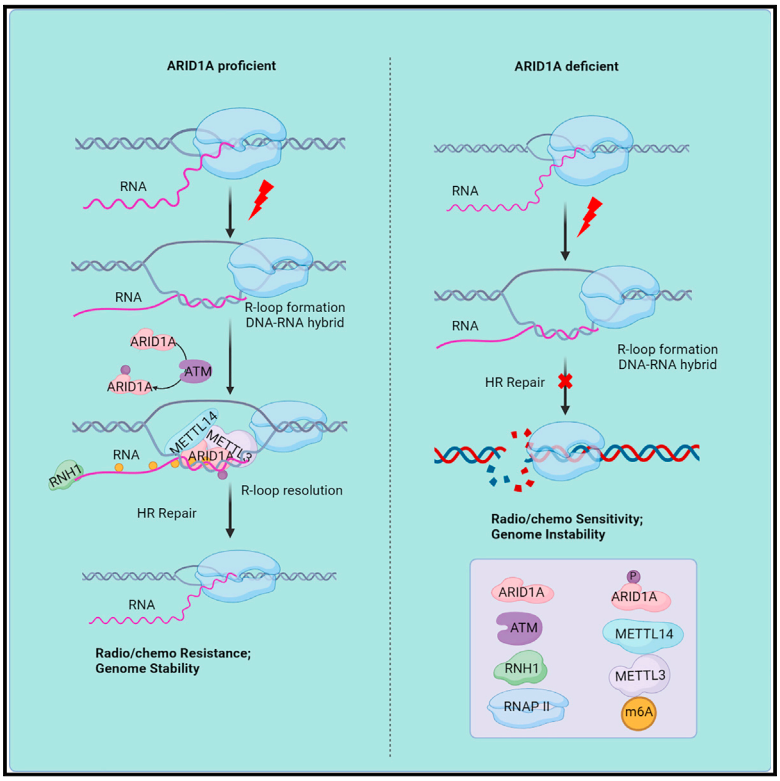

Highlights

- ARID1A recognizes R-loops and facilitates R-loop resolution at DSBs
- ARID1A is recruited to R-loop in an ATM-dependent manner
- ARID1A facilitates R-loop m6A modification by recruiting METTL3 to DSBs
- RNase H1 preferentially binds to m6A-modified R-loops

Authors

Jun Zhang, Feng Chen, Ming Tang, ..., Xingzhi Xu, Monika Gullerova, Wei-Guo Zhu

Correspondence

zhuweiguo@szu.edu.cn

In brief

Zhang et al. show that ARID1A plays a role in recognizing R-loops and facilitating their resolution by recruiting METTL3 to local DSBs to initiate R-loop m6A modification. In this context, m6A modification determines the fate of R-loops by efficiently recruiting RNase H1 during DNA damage repair.

Zhang et al., 2024, Cell Reports *43*, 113779
February 27, 2024
https://doi.org/10.1016/j.celrep.2024.113779

CellPress

Cell Reports

CellPress
OPEN ACCESS

Article

The ARID1A-METTL3-m6A axis ensures effective RNase H1-mediated resolution of R-loops and genome stability

Jun Zhang,[1,8] Feng Chen,[1,8] Ming Tang,[2] Wenchao Xu,[1] Yuan Tian,[1] Zhichao Liu,[3] Yuxin Shu,[1] Hui Yang,[1] Qian Zhu,[1] Xiaopeng Lu,[1] Bin Peng,[4] Xiangyu Liu,[1] Xingzhi Xu,[4] Monika Gullerova,[3] and Wei-Guo Zhu[1,5,6,7,9,*]

[1]International Cancer Center, Guangdong Key Laboratory of Genome Instability and Human Disease Prevention, Department of Biochemistry and Molecular Biology, Shenzhen University Medical School, Shenzhen 518055, China
[2]Shanghai Key Laboratory of Maternal Fetal Medicine, Shanghai First Maternity and Infant Hospital, School of Medicine, Tongji University, Shanghai 200092, China
[3]Sir William Dunn School of Pathology, South Parks Road, Oxford OX1 3RE, UK
[4]International Cancer Center, Guangdong Key Laboratory of Genome Instability and Human Disease Prevention, Department of Cell Biology and Medical Genetics, Shenzhen University Medical School, Shenzhen 518055, China
[5]Marshall Laboratory of Biomedical Engineering, Shenzhen University Medical School, Shenzhen 518055, China
[6]School of Basic Medical Sciences, Wannan Medical College, Wuhu, Anhui 241002, China
[7]Department of Biochemistry and Molecular Biology, Peking University Health Science Centre, Beijing 100191, China
[8]These authors contributed equally
[9]Lead contact
*Correspondence: zhuweiguo@szu.edu.cn
https://doi.org/10.1016/j.celrep.2024.113779

SUMMARY

R-loops are three-stranded structures that can pose threats to genome stability. RNase H1 precisely recognizes R-loops to drive their resolution within the genome, but the underlying mechanism is unclear. Here, we report that ARID1A recognizes R-loops with high affinity in an ATM-dependent manner. ARID1A recruits METTL3 and METTL14 to the R-loop, leading to the m6A methylation of R-loop RNA. This m6A modification facilitates the recruitment of RNase H1 to the R-loop, driving its resolution and promoting DNA end resection at DSBs, thereby ensuring genome stability. Depletion of ARID1A, METTL3, or METTL14 leads to R-loop accumulation and reduced cell survival upon exposure to cytotoxic agents. Therefore, ARID1A, METTL3, and METTL14 function in a coordinated, temporal order at DSB sites to recruit RNase H1 and to ensure efficient R-loop resolution. Given the association of high ARID1A levels with resistance to genotoxic therapies in patients, these findings open avenues for exploring potential therapeutic strategies for cancers with ARID1A abnormalities.

INTRODUCTION

The nascent RNA transcript can rehybridize with the DNA template, displacing non-template single-stranded DNA and forming a 3-stranded nucleic acid structure known as an R-loop.[1–3] R-loops have diverse functions essential for eukaryotic physiology.[1,3,4] The excessive accumulation of R-loops at specific genomic loci can also pose a significant threat to genomic stability and lead to chromosome translocation and ultimately produce double-stranded breaks (DSBs).[4,5] Excessive R-loop accumulation correlates with the pathogenesis of multiple genomic instability-based human diseases.[6–10] As such, to maintain genome stability, cells have evolved various strategies to resolve unexpected R-loop formation, including DNA/RNA helicases that unwind the DNA/RNA hybrid,[11,12] pre-mRNA processing factors that bind with mRNA transcripts to prevent the re-hybridization of the nascent RNA with the template DNA,[13,14] and additionally, the ribonuclease (RNase) H enzymes that degrade R-loop RNA chains.[15–18] Yet despite the identification of many factors involved in R-loop resolution, it is still unclear how R-loops are intrinsically recognized and precisely resolved to maintain genome stability.

RNase H is one of the most important factors contributing to R-loop clearance and is a conserved endonuclease that hydrolyzes the phosphodiester backbone of the RNA moiety in RNA-DNA hybrids.[19] RNase H is divided into two classes, namely RNase H1 and RNase H2, and both RNase H1 and RNase H2 have a role in suppressing R-loops in the genome.[9,20] Recent studies have suggested that RNase H1 overexpression is sufficient to resolve R-loops during genome stress.[19,21] RNase H1 recruitment to R-loop-prone sites was recently identified based on its binding with RPA, a single-stranded DNA (ssDNA)-binding protein. Purified RPA directly enhances the association of RNase H1 with RNA-DNA hybrids and stimulates RNase H1 activity on R-loops *in vitro*.[22] Furthermore, RNase H1 was reported to be recruited by TonEBP.[23] Despite these advances, how the R-loop-processing enzyme RNase H1 recognizes R-loops and how it is regulated need to be explained.

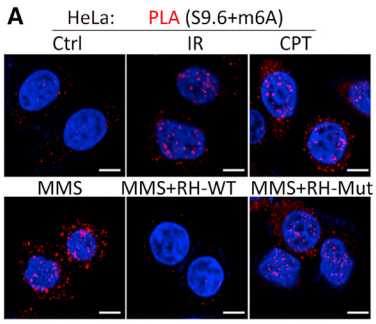

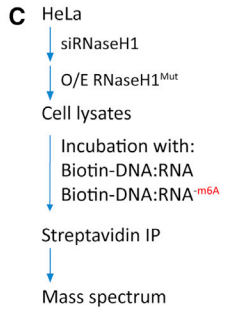

Protein Name	MW	Normalized Intensity DNA:RNA	Normalized Intensity DNA:RNA-m6A
RNaseH1	32.064	0.726357	1.841186
hnRNPA2B1	37.429	0.563684	1.733689
IGF2BP1	63.484	0.472965	1.227035
BRIX1	41.401	0.63891	1.36109
CHD1	196.69	0.770298	1.229702
CCDC47	55.873	0.8836	1.1164
ADAR	136.06	0.909972	1.090028
TOP2A	174.38	1.239689	1.329128
UHRF1	89.813	0.875945	1.024055
DDX27	89.834	0.939445	0.884873
DDX21	87.343	1.229845	1.220829
MRTO4	27.56	1.143746	0.856254
ARID1A	242.04	0.186961	0.179996

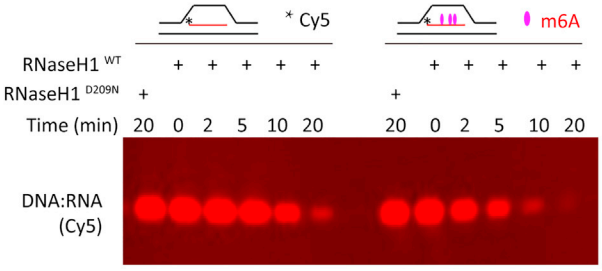

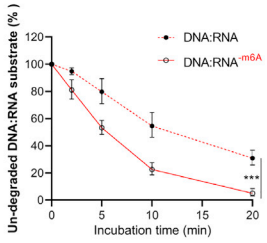

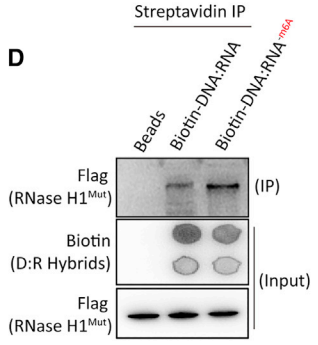

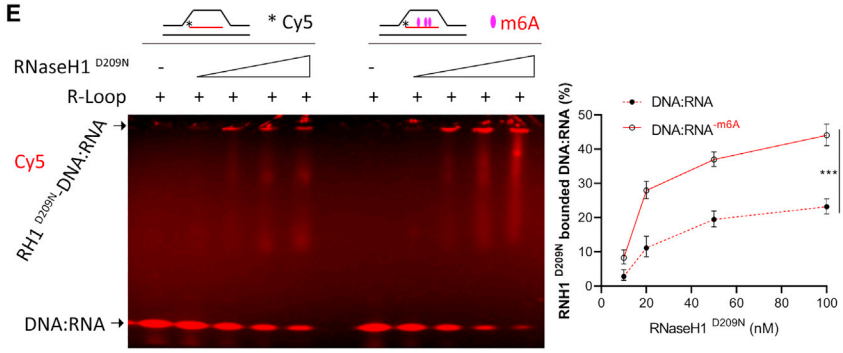

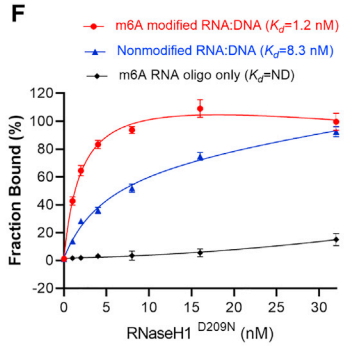

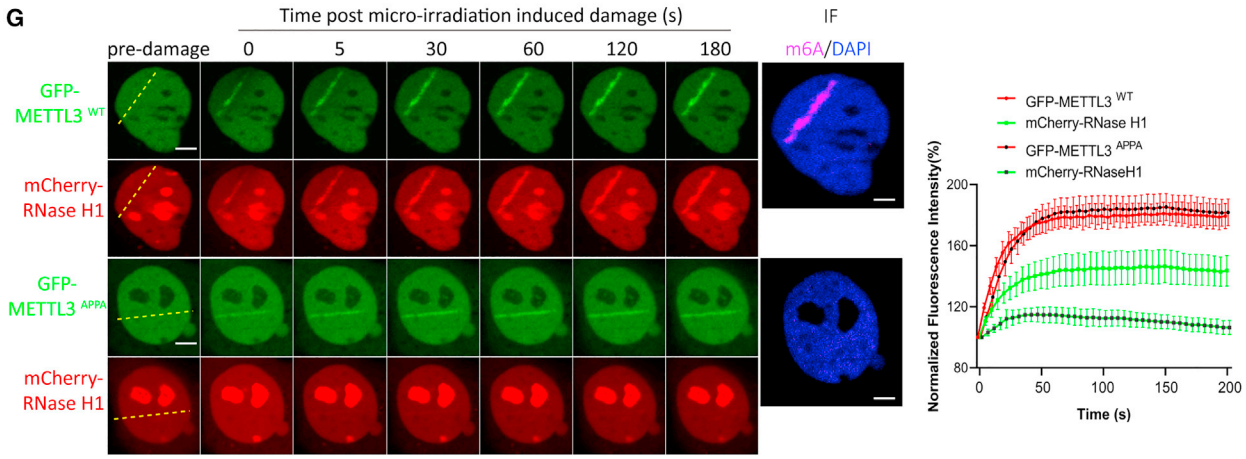

(legend on next page)

Methylation on the N6 position of adenosine (m6A), which is catalyzed by the methyltransferases METTL3 and METTL14, is one of the most abundant modifications that occur on mRNAs.[24–26] Moreover, growing evidence has demonstrated that m6A methylation is a critical mediator of DNA damage repair. m6A RNA methylation serves as a platform to recruit Pol κ to DNA damage sites.[27] m6A methylation on R-loop RNA might also be critical for governing R-loop stability by either stabilizing or clearing R-loops.[28–30] The m6A-containing R-loop accumulates during the G2/M phase and is depleted at the G0/G1 phase of the cell cycle; the m6A modification promotes R-loop RNA degradation, suggesting that m6A regulates the clearance of an R-loop to safeguard genomic stability.[28] In addition, METTL3 phosphorylation by ATM catalyzes the m6A modification on R-loop RNA as a prerequisite step for R-loop accumulation at DSBs, which further facilitates homologous recombination (HR) repair.[29] Given the dual role of m6A in regulating R-loop biology, elucidating the precise regulation mechanisms of m6A and R-loop during the DNA damage process is critical to understanding how DNA repair is uniquely regulated in a temporal and spatial manner.

AT-rich interactive domain 1A (ARID1A) is an SWI/SNF family member that regulates gene transcription by altering chromatin structure via its helicase and ATPase activities.[31] ARID1A is frequently mutated and is a poor prognostic marker in various human cancers.[31,32] The mutation frequency of ARID1A ranges from 10% to 60% across multiple tumor lineages, including ovarian carcinoma, gastric and pancreatic cancer, and cholangiocarcinoma, among others.[32–34] ARID1A participates in genome maintenance by rapidly localizing to damaged sites, clearing nucleosome occupancy, and physically facilitating local recruitment of DNA repair factors to stress regions.[35–40] Despite previous studies demonstrating the involvement of ARID1A in genome stability maintenance, there is still a need for a deeper understanding of the specific mechanisms by which ARID1A contributes to DNA damage repair pathways. In particular, there is a lack of knowledge regarding the molecular events that regulate the pathogenesis associated with ARID1A deficiency and the mechanisms by which ARID1A ensures the maintenance of DNA integrity in response to both endogenous and environmental challenges that lead to DNA damage.

Here we aimed to address the mechanisms underlying the resolution of R-loops in response to DNA damage and its significance in genotoxic treatments. Specifically, we provide evidence supporting the hypotheses that ARID1A plays a crucial role in recognizing R-loops induced by DNA damage and facilitating their resolution to maintain genome stability, by recruiting METTL3 and METTL14 to local DNA damage sites to initiate the m6A RNA methylation. Delineating the precise mechanisms of this process will further strengthen our understanding on the relevance of R-loop biology in the context of genotoxic treatment approaches.

RESULTS

RNase H1 preferentially binds m6A-modified R-loops and catalyzes R-loop resolution

RNA methylation frequently occurs in both nascent messenger RNA and R-loops.[41,42] To understand whether RNA methylation is involved in DNA damage response, we examined RNA methylation using specific antibodies against N7-methylguanosine (m7G), N6-methyladenosine (m6A), and N5-methylcytosine (m5C) after DNA damage and found that all the three types of RNA methylation levels were increased in response to DNA damage (Figure S1A). To further explore whether RNA methylations occurred in the R-loops, we performed a proximity ligation assay (PLA) to visualize and quantify the *in situ* interactions. Remarkably, we observed increased numbers of PLA foci (red dots) corresponding to *in situ* endogenous interactions between m6A (Figure 1A) or m5C (Figure S1B) and R-loops in response to DNA damage. The interaction between the R-loop and m7G seems to not be related to DNA damage (Figure S1B). These data suggest that m5C and m6A but not m7G RNA modification occurred on the R-loop prone in a DNA-damage-dependent manner. The specificity of these RNA methylation antibodies was verified by knocking down the methyltransferases NSUN2, METTL3, and METTL1, respectively (Figure S1C).

To test whether m6A RNA modification was also involved in modulating R-loop stability, we synthesized a Cy5-labeled RNA oligo, m5C, as well as m6A-modified RNA oligos, and we annealed these oligos with a DNA oligo to generate an R-loop-like structure comprising two arms of double-stranded DNA (dsDNA, 30 bp), a bubble of ssDNA (31 nt) in the middle, and an RNA:DNA hybrid (25 nt, R-loop) in the bubble. This R-loop structure was validated by S9.6- DNA-RNA immunoprecipitation (DRIP)-qPCR and m6A-DIP-qPCR analysis (Figures S1D and S1E). After incubating the Cy5-R-loop products with gradually increasing amounts of purified

Figure 1. RNase H1 preferentially binds m6A-modified R-loops and catalyzes R-loop resolution

(A) *In situ* PLA of the interaction between S9.6 and m6A in HeLa cells treated with different DNA-damaging agents. The PLA foci were observed after staining with S9.6 and m6A antibodies. ***$p < 0.001$.

(B) The stability of R-loops was measured by native-PAGE. The Cy5-labeled R-loop and R-loop^{m6A} substrates were incubated with RNase H1^{WT} or RNase H1^{D209N} (5 nM) *in vitro* for the indicated times. The products were subjected to native-PAGE, and the captured images were analyzed using a fluorescence imaging system. ***$p < 0.001$.

(C) HeLa cells were transfected with siRNA, overexpressed with FLAG-RNase H1^{Mut} construct, and subjected for DNA:RNA hybrid IP. The table shows the number of peptides and the percentage coverage of identified candidates.

(D) The above IP products by DNA:RNA hybrids were analyzed by western blotting assay using the indicated specific antibodies (anti-biotin).

(E) The binding affinity of R-loops was measured by EMSA. The Cy5-labeled R-loop and R-loop^{m6A} substrates were incubated with RNase H1^{D209N} (5 nM) *in vitro* for the 20 min. The RNase H1^{D209N}:R-loop complex as well as free R-loops were captured and analyzed by a fluorescence imaging system. ***$p < 0.001$.

(F) An MST assay showing the affinity of His-RNase H1 for m6A-modifed and unmodified R-loops. The corrected fraction bound curve was shown.

(G) RNase H1 accumulation dynamics at DSBs was monitored by laser microirradiation-coupled live-cell imaging. The mCherry and GFP fluorescent intensity at DSBs was quantified by ImageJ.

Each assay was conducted in a minimum of three independent experiments. Data represent the means ± SEM for (A). Scale bar: 10 μM for (A) and 20 μM for (G).

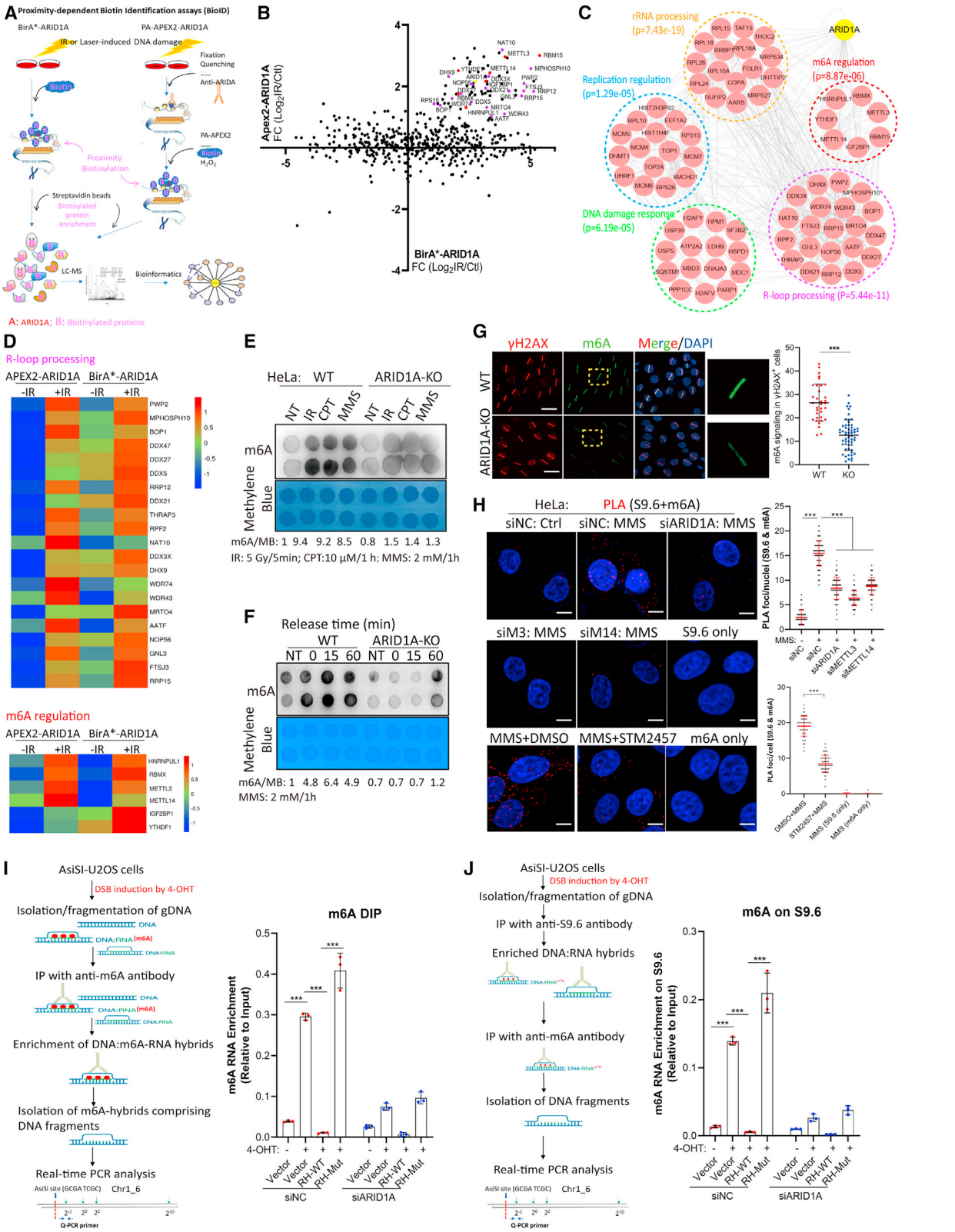

(legend on next page)

RNase H1 *in vitro* for 10 min, we observed that m6A- but not m5C-modified R-loops showed a markedly decreased pattern, suggesting that m6A modification favors the degradation of R-loops (Figure S1F). We further incubated the m6A-modified R-loop with RNase $H1^{WT}$ and RNase $H1^{D209N}$ (catalytically inactive mutant), and we found that RNase $H1^{WT}$ cleaved RNA in the m6A-modified R-loop more rapidly (Figure 1B).

To test whether the m6A-modified R-loop enhanced the binding of RNase H1 to the R-loop and facilitated its degradation, we performed a DNA:RNA hybrid pull-down assay and analyzed its potential interactomes (Figure 1C, left). By mass spectrometry analysis, we identified many interactors that bind to R-loops, and RNase H1 was identified to bind with m6A-modified R- loops in high affinity (Figures 1C, right, and 1D). We performed an *in vitro* electrophoretic mobility shift assay (EMSA) and further confirmed that the binding affinity of RNase $H1^{D209N}$ to m6A-modified R-loops was much higher than unmodified R-loops. Specifically, we observed increased levels of RNase H1-DNA:RNA complex formation and decreased levels of free DNA:RNA hybrid (Figure 1E). The high binding affinity of RNase H1 to m6A-modified R-loops was further confirmed by the microscale thermophoresis (MST) assay, as m6A-modified R-loops have a low dissociation constant (Kd) (Kd = 1.2) value compared with the unmodified R-loops (Kd = 8.3) (Figure 1F). These results together suggest that RNase H1 preferentially binds to m6A-modified R-loops.

We next diminished the RNA m6A methylation by expressing a catalytically inactive METTL3, in which D395 and W398 were mutated to A (DPPW to APPA) and tested the dynamic of RNase H1 recruitment to DSBs in a laser-induced DNA damage system. By co-expressing GFP-$METTL3^{WT}$ or $METTL3^{APPA}$ with mCherry-RNase H1, we found that the dynamic recruitment of mCherry-RNase H1 only occurred in $METTL3^{WT}$ but not in $METTL3^{APPA}$ cells (Figure 1G). These findings suggest that METTL3-catalyzed R-loop RNA m6A methylation has a vital role in RNase H1 recruitment and R-loop resolution in DNA damage sites.

ARID1A facilitates damage-induced R-loop m6A modification on DSB-flanking chromatin in response to DNA damage

We asked whether ARID1A is involved in R-loop regulation since ARID1A is a potential binding partner to R-loops (Figure 1C, right). We performed proximity-dependent biotin identification assays to isolate the potential interactomes of ARID1A using either BirA*[43] or APEX approaches[44] that serve as biotin ligase to biotinylate proteins in close proximity to ARID1A (Figure 2A). After microirradiation, we found that ARID1A was efficiently recruited to laser stripes accompanied by biotin signals (Figures S2A and S2B). Similar results were also observed with APEX-ARID1A (Figures S2D and S2E), suggesting that both BirA*-ARID1A and APEX-ARID1A induce biotinylation of proximal proteins. We further captured and identified the biotinylated proteins and found several overlapping proteins in the above-mentioned two independent systems (Figure 2B). A functional relationship was demonstrated by clusters including R-loop processing and m6A regulation (Figures 2C and 2D). Furthermore, the representative identified proteins were validated by western blotting, including MDC1, PARP1, UHRF1, and METTL3 (Figures S2C and S2F).

We experimentally explored the possible roles of ARID1A on RNA m6A modification and observed that total m6A levels in ARID1A-deficient cells markedly decreased (about 85%) in response to DNA damage (Figures 2E and 2F). We further stained the m6A levels at the γH2AX tracks in laser stripes and observed that local m6A levels at DSBs were significantly decreased upon ARID1A depletion (Figure 2G) This conclusion was further validated by a quantitative m6A-DNA immunoprecipitation (m6A-DIP) assay in the 4-OHT-induced site-specific DSB system. We observed that 4-OHT treatment markedly enhanced (~5-fold) the m6A levels on DSBs, which was significantly inhibited upon ARID1A knockdown in A*si*SI-U2OS cells (Figure 2I).

We further explored the m6A modification that occurred in the R-loop-prone sites by PLA analysis, and we observed positive PLA foci between m6A and R-loops in response to DNA damage, which was abolished by depletion of ARID1A, the m6A methyltransferase METTLs, as well as METTL3 enzymatic inhibitor STM2457 (Figures 2H and S2G). By a two-round DRIP/DIP assay (S9.6 DRIP followed by m6A DIP), a quantitative examination of the levels of m6A on S9.6 at the DSBs further showed that the m6A levels on S9.6 were enhanced ~9-fold upon 4-OHT treatment, and this increase was reversed upon overexpression of an RNase $H1^{WT}$ in ARID1A-expressing cells (Figure 2J). These findings suggest that ARID1A plays an important role in R-loop RNA m6A modification upon DNA damage.

Figure 2. ARID1A facilitates damage-induced R-loop m6A modification on DSB-flanking chromatin in response to DNA damage

(A) Workflow of the ARID1A interactome analysis by proximity-dependent biotin identification (BioID) assays.

(B) Overlap and distribution of the ARID1A interactome identified by Apex2-ARID1A and BirA*-ARID1A approaches.

(C) Network analysis of ARID1A interactomes. Individual proteins are shown as nodes, and edges indicate interactions retrieved from the STRING database.

(D) Heatmap of the ARID1A-interacting proteins classified on the basis of their functionality in R-loop processing (upper) and m6A regulation (lower).

(E and F) Dot blot analysis of m6A levels after DNA damage stimulation. The treated cells were produced by lysis, and chromatin-associated RNAs were extracted and subjected to dot blot analysis using an m6A-specific antibody. Methylene blue staining was used as a loading control.

(G) Immunofluorescence staining showing the m6A and γH2AX signal in laser microirradiation-induced DNA damage sites in HeLa and ARID1A-KO cells. The m6A density at DSB stripes was quantified using ImageJ. ***$p < 0.001$.

(H) *In situ* PLA of the interaction between S9.6 and m6A in HeLa cells transfected with different siRNAs. The PLA foci were observed after staining with S9.6 and m6A antibodies after MMS (2 mM for 1 h) treatment. ***$p < 0.001$.

(I) Schematic illustrating the m6A DIP technique (left), showing the enrichment of m6A-modified RNA at DSB sites induced by 4-OHT (500 nM) in the AsiSI-U2OS system after cells were transfected as indicated (right). ***$p < 0.001$.

(J) Schematic illustrating the DRIP (R-loop)-re-DIP (m6A) technique (left), showing the enrichment of m6A-modified RNA of R-loops at DSB sites in the AsiSI-U2OS system. ***$p < 0.001$.

Each assay was conducted in a minimum of three independent experiments. Data represent the means ± SEM for (G and H) and means ± SD for (I and J). Scale bar: 10 μM for (G) and (H).

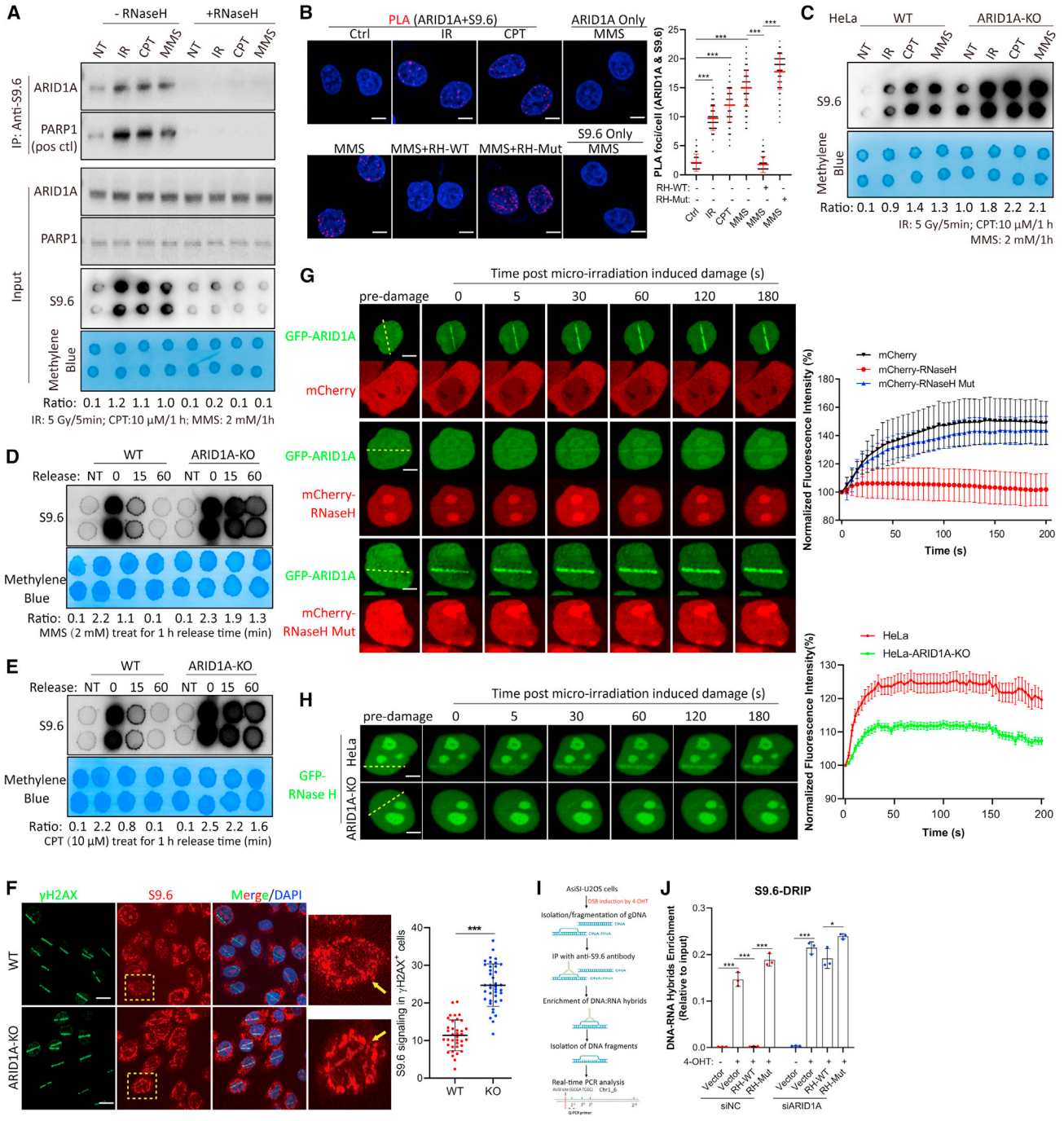

Figure 3. Chromatin-enriched ARID1A recognizes R-loops and facilitates R-loop resolution at DSBs

(A) R-loop immunoprecipitation analysis of the endogenous interaction between ARID1A and R-loops. The treated cells were produced by lysis, and genomic DNAs were extracted and pretreated with either RNase H1 enzyme or not, and then the products were subjected to immunoprecipitation using an anti-S9.6 antibody.

(B) *In situ* PLA of the interaction between S9.6 and ARID1A in HeLa cells. The PLA foci were observed after staining with S9.6 and ARID1A antibodies after treatment as indicated. ***p < 0.001.

(C) Dot blot analysis of R-loop levels at HeLa and ARID1A-deficient cells after DNA damage treatment. The cellular genomic DNA was extracted and subjected to dot blot analysis. Methylene blue staining was used as a loading control.

(D and E) Dot blot analysis of R-loop levels in HeLa and ARID1A-deficient cells after DNA damage treatment. The cellular genomic DNA was extracted and subjected to dot blot analysis. Methylene blue staining was used as a loading control.

(legend continued on next page)

Chromatin-enriched ARID1A recognizes R-loops and facilitates R-loop resolution at DSBs

We next asked whether ARID1A is recruited to DSBs to exert its role in m6A modification. We isolated chromatin and found ARID1A recruitment occurs in a dose- and time-dependent manner to DNA damage (Figures S3A and S3B). This finding was confirmed by co-staining endogenous ARID1A and γH2AX after laser-generated DNA damage (Figure S3C). Next, we overexpressed GFP-ARID1A in multiple cancer cell lines and found that laser microirradiation triggered swift accumulation of GFP-ARID1A at DNA damage sites (Figure S3D). Thus, we conclude that ARID1A is recruited to DNA damage sites. We further conducted an R-loop IP and found that ARID1A was pulled down by R-loops after DNA damage; digestion of the R-loop by RNase H abolished this interaction (Figure 3A). Of note, we used PARP1 as a positive control.[11] This interaction was further confirmed by PLA (Figure 3B), suggesting that chromatin-bound ARID1A interacts with R-loops in response to DNA damage.

To explore the role of ARID1A in R-loop regulation, we examined the R-loop levels in WT and ARID1A-deficient cells following DNA damage. We found that R-loop levels accumulated in ARID1A-deficient cells (Figure 3C). To monitor the kinetics of R-loop accumulation, we treated the cells with DNA damage agents and released them for the indicated times. ARID1A deficiency delayed R-loop clearance (Figures 3D and 3E), suggesting that ARID1A is important for R-loop clearance. This observation was further validated by staining of R-loops at laser-induced DSBs (Figure 3F). We further co-transfected GFP-ARID1A and mCherry-RNase H1 and tracked the dynamics of GFP-ARID1A recruitment to laser stripes. GFP-ARID1A recruitment was abolished only in cells co-transfected with mCherry-RNase H1 (Figure 3G), indicating that clearance of R-loops by RNase H1 diminished ARID1A loading to DSBs. Moreover, we found that an ARID1A deficiency abolished GFP-RNase H1 recruitment to laser microirradiation-induced DSBs (Figure 3H), further supporting the conclusion that ARID1A is required for R-loop clearance.

Finally, to quantify R-loop levels at DSBs, we reduced ARID1A levels by siRNA in A*si*SI-U2OS cells and induced DSBs with 4-OHT. We then quantified R-loop levels by DRIP assay using the anti-RNA:DNA hybrid S9.6 antibody following the workflow shown in Figure 3I. As shown in Figure 3J, knockdown of ARID1A increased the R-loop levels around DSBs by ~2-fold after DSB induction by 4-OHT treatment, and the enhanced R-loop levels were resolved by overexpressing WT-RNase H1, but not Mut-RNase H1, in ARID1A-proficient cells. Furthermore, the RNase H1-mediated R-loop resolution was remarkedly diminished in ARID1A-deficient cells, as ARID1A deficiency abolished the RNase H1 loading to DSBs (Figure 3J). These data together suggest that chromatin-enriched ARID1A recognizes R-loops and facilitates R-loop resolution at DSBs.

Chromatin-enriched ARID1A recruits METTL3/14 to R-loop to facilitate R-loop RNA m6A modification

We experimentally examined the endogenous interactions among ARID1A, METTL3, and MELLT14 based on the interactome identification and found that, indeed, ARID1A, METTL3, and METTL14 interacted with each other in response to DNA damage (Figures S4A–S4D). We further observed that ARID1A depletion abolished the METLL3 and METTL14 recruitment to chromatin by either chromatin fraction isolation (Figure 4A) or by laser-coupled live-cell imaging (Figures 4B, 4C, S4E, and S4F). Thus, ARID1A is required for METTL3 and METTL14 recruitment to damage sites.

Furthermore, we found that there was no significant difference in GFP-ARID1A recruitment to laser-induced DSB stripes in METTLs-depleted cells (Figure S4G), suggesting that m6A methylation has no effect on ARID1A recruitment. We then performed a PLA assay to observe *in situ* ARID1A and R-loop colocalization and found that METTL3 and METTL14 downregulation also had no significant effect on the number of PLA foci (Figure 4D). Thus, we presume that R-loop m6A methylation is not required for ARID1A recognition of R-loops. Furthermore, we found that the R-loop levels were remarkedly increased, while the m6A levels showed no significant differences in ARID1A-depleted cells with overexpression of METTL3 and METTL14 (Figure 4E). This conclusion was further confirmed by a two-round DRIP-re-DIP assay (Figure 4F), which showed that the m6A levels on R-loops were not increased in ARID1A-deficient cells even with overexpression of METTL3 and METTL14. Together, these data suggest that ARID1A-METTL3/14 function in a temporal order to regulate R-loop m6A levels at DSBs.

ATM-dependent ARID1A recruitment to DSBs is required for R-loop resolution

To explore the regulatory signaling that facilitates ARID1A recruitment to chromatin, we treated cells with multiple inhibitors and found that chromatin ARID1A was markedly reversed only with the ATM inhibitor KU-55933, suggesting that ATM kinase activity is required for ARID1A chromatin recruitment (Figures S5A–S5C). This conclusion was further confirmed by staining of endogenous ARID1A at laser stripes (Figure 5A). We further examined ARID1A phosphorylation using an ATM substrate antibody, phospho-S/TQ, and we found that ARID1A phosphorylation was elevated following DNA damage, which was reversed upon treatment with an ATM inhibitor (Figures 5B and 5C). Thus, ARID1A is a potential substrate of ATM kinase. We then took advantage of the A*si*SI-ER U2OS platform to dissect the role of ARID1A phosphorylation in chromatin distribution. We focused our analysis on Chr 1_6 and Chr 1_12 since these sites are sensitive to 4-OHT induction and undergo robust DNA damage.[45,46] Chromatin immunoprecipitation (ChIP) assays revealed

(F) Immunofluorescence staining showing S9.6 and γH2AX signals at laser microirradiation-induced DSBs in HeLa and ARID1A-KO cells. The S9.6 density at DSB stripes was quantified with ImageJ. ***$p < 0.001$.
(G and H) The dynamics of ARID1A and RNase H1 accumulation at DSBs was monitored by laser microirradiation-coupled live-cell imaging.
(I and J) Schematic illustrating the R-loop DRIP technique (I). The S9.6 DRIP shows the enrichment of R-loops at DSB sites induced by 4-OHT (500 nM) in the AsiSI-U2OS system after cells were transfected as indicated (J). *$p < 0.05$, ***$p < 0.001$.
Each assay was conducted in a minimum of three independent experiments. Data represent the means ± SEM for (B and F) and means ± SD for (I and J). Scale bar: 10 μM for (B and F) and 20 μM for (G and H).

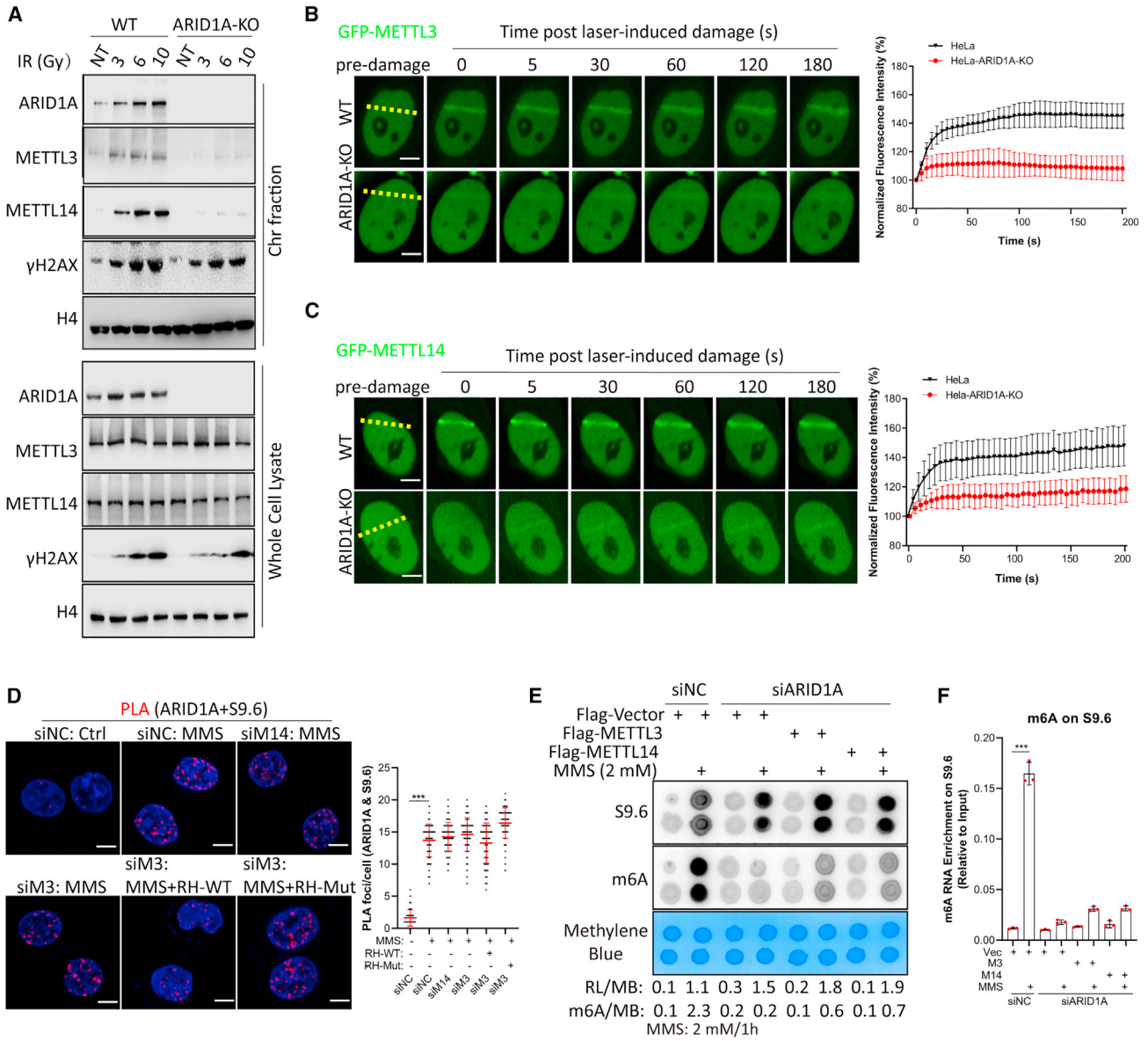

Figure 4. ARID1A recruits METTL3/14 to R-loop and facilitates R-loop RNA m6A modification

(A) HeLa cells were exposed to different doses of IR. Then, the chromatin fractions were isolated 30 min after treatment, and the cell extracts were analyzed by western blotting.

(B and C) The dynamics of METTL3 accumulation at DSBs was monitored by laser microirradiation-coupled live-cell imaging in HeLa and ARID1A-KO cells expressing GFP-METTL3 (B) and GFP-METTL14 (C). The GFP intensity at DSBs was quantified with ImageJ.

(D) *In situ* PLA of the interaction between S9.6 and ARID1A in HeLa cells transfected with different siRNAs. The PLA foci were observed after staining with S9.6 and ARID1A antibodies. ***$p < 0.001$.

(E) Dot blot analysis of S9.6 and m6A levels at HeLa and ARID1A-knockdown cells after MMS treatment; the cells were extracted, and samplers were subjected to dot blot analysis. Methylene blue staining was used as a loading control.

(F) DRIP-re-DIP showing the enrichment of m6A-modified RNA of R-loops at DSB sites induced by 4-OHT (500 nM) in the AsiSI-U2OS system after cells were transfected as indicated. ***$p < 0.001$.

Each assay was conducted in a minimum of three independent experiments. Data represent the means ± SEM for (D) and means ± SD for (F). Scale bar: 10 μM for (D) and 20 μM for (B) and (C).

that 4-OHT treatment induced ~4-fold enrichment of ARID1A around DSBs up to a distance of 5 kb flanking A*si*SI sites (Chr1_6 and 12), which was significantly suppressed by ATM inhibitor treatment (Figure 5D). In accordance with these findings, we found the significant and rapid accumulation of GFP-ARID1A in the laser stripes was decreased in ATM-inactivated cells following microirradiation (Figure 5E). This conclusion was further confirmed by the overexpression of ATM mutants that

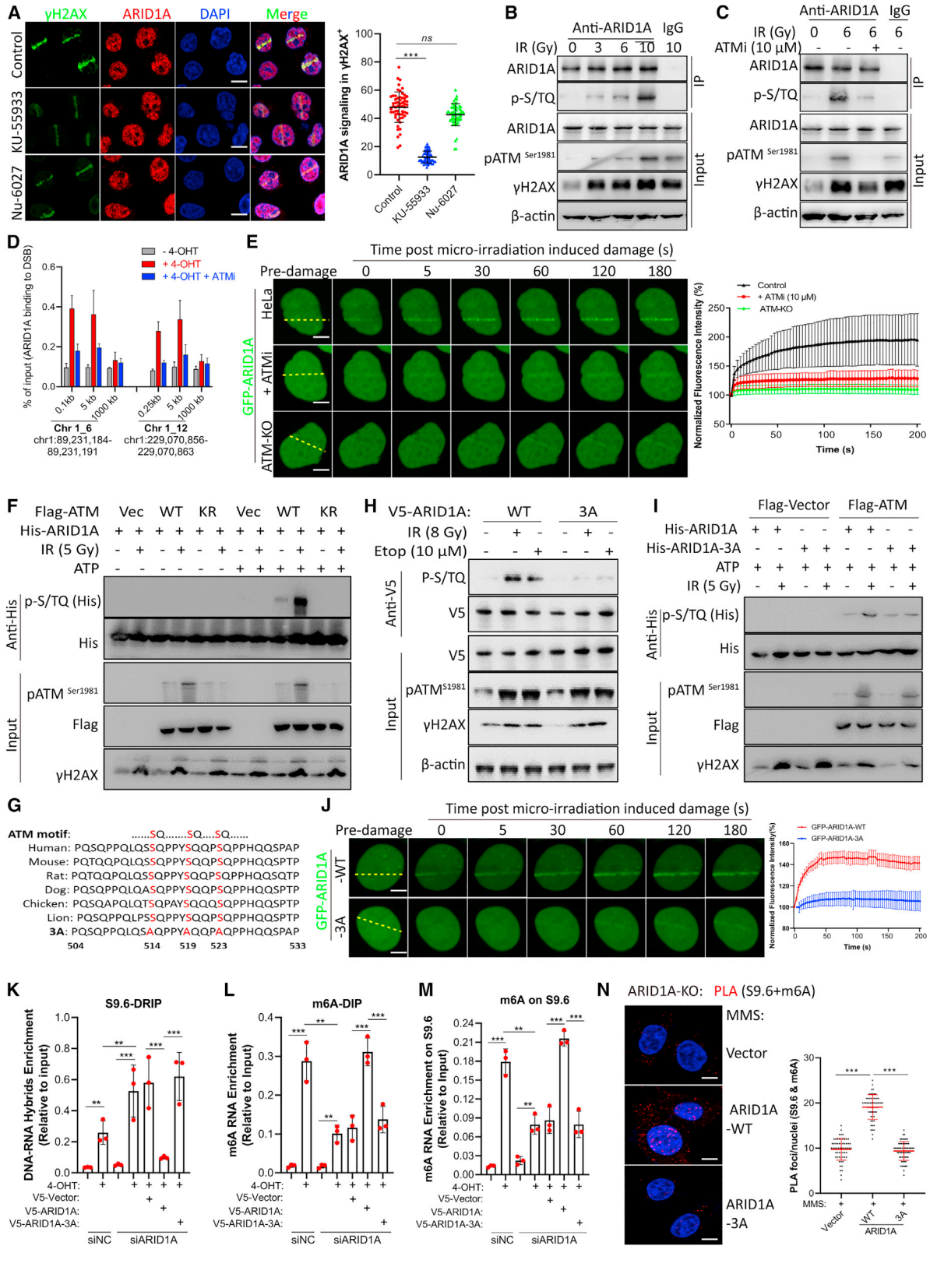

(legend on next page)

mimic activation (K3016Q) and inactivation (K3016R) (Figure S5D). These results suggest that ARID1A is recruited to chromatin in an ATM-kinase-activity-dependent manner.

By overexpressing different regions of ARID1A, we found that only the constructs that covered 1–595^{aa} were phosphorylated in response to DNA damage (Figure S5E). We then performed an *in vitro* kinase activity assay by incubating the recombinant His-ARID1A with cellular purified FLAG-ATM constructs. The data showed that only ATM^{WT} could markedly promote ARID1A phosphorylation (Figures S5F and 5F). Using STRAP (Structure based Sequences Alignment Program), we generated multiple sequence alignments of this region from several species and revealed an evolutionarily conserved region with repeated S/TQ residues serving as potential ATM substrate motifs (Figure 5G). After generating an ARID1A^{3A} mutation, we found that ATM-mediated phosphorylation of ARID1A was abolished both *in vivo* and *in vitro* (Figures 5H and 5I). Moreover, ARID1A-3A mutation prevented ARID1A enrichment at microirradiation-induced DSBs (Figure 5J). Functional characterization of mutated ARID1A showed that rescuing ARID1A-deficient cells with ARID1A^{3A} failed to enhance S9.6 levels (Figure 5K), m6A levels (Figure 5L), and m6A-modified R-loops (Figures 5M and 5N) at DSBs. To further characterize whether this mechanism is specific to R-loop resolution occurring at DSBs, we further induced R-loop formation by using spliceosome inhibitor Plad-B, and our results showed that the ARID1A was not recruited to this non-DSB-induced R-loop (Figure S5G). Thus, ARID1A is a bona fide ATM substrate in response to DSBs, and ARID1A phosphorylation by ATM is required for its recruitment to chromatin.

ARID1A-mediated R-loop resolution enables end resection and DNA damage repair

We measured the abundance of ssDNA intermediates, as R-loop resolution leads to release of the DNA strand. Genomic DNA harvested following A*si*SI induction was treated with *BsrGI*, to digest dsDNAs, and *Hind III* digested product was used as a negative control (Figure 6A). A*si*SI induction resulted in a substantial increase in ssDNA abundance. Meanwhile, disturbing R-loop-m6A levels by interfering with the ARID1A-METTL3/14 axis significantly abolished ssDNA abundance at DNA damage sites (Chr 1_6), similar to CtIP-inactivated cells (Figure 6B). The ssDNA levels detected near DSB proximal regions were more abundant than those at distant regions from the damage sites. Accordingly, we observed that overexpression of ARID1A^{WT}, but not ARID1A,^{3A} increased the ssDNA levels near DNA damage sites 6-fold (Figure 6C). Similarly, overexpression of RNase H1^{WT} to resolve R-loops also increased the ssDNA abundance in parental cells (Figure 6D). Thus ARID1A-mediated R-loop resolution seems to have a vital role in DNA end resection.

We then carried out immunostaining to analyze the recruitment of HR repair factors. ARID1A depletion significantly delayed RPA70 and RAD51 recruitment to DSBs, suggesting that ARID1A-mediated R-loop resolution is required for end resection by controlling the RPA70 and RAD51 loading (Figures 6E and 6F). We then further monitored the DSB repair efficiency and observed that inactivation of ARID1A caused a significant delay in the recovery of γH2AX levels (Figure 6G); however, expression of an RNase H1^{WT} but not RNase H1^{Mut} significantly accelerated DNA damage repair, indicating that ARID1A-mediated R-loop resolution plays vital roles in DNA damage repair. We further quantified HR repair efficiency in an I-SceI-induced DNA damage repair system. Disrupting the R-loop clearance process by interfering with ARID1A, METTL3, and METTL14, in turn, attenuated HR repair efficiency (Figure 6H). Overexpression of a ARID1A^{WT}, but not ARID1A^{3A}, rescued the repair efficiency that was abolished by ARID1A inactivation (Figure 6I). Furthermore, RNase H1^{WT} could enhance the repair efficiency by ∼1.8-fold in cells with ARID1A expression, whereas RNase H1^{Mut} failed to do so (Figure 6J). These data support that ARID1A facilitates DNA damage repair through R-loop clearance and accelerates DSB end resection.

ARID1A mediates genome stability maintenance and resistance to DNA-damaging treatment in cellular and clinical patients

To understand the biological relevance of ARID1A in cancer cells, we examined the survival ability of different clones after irradiation. Colony-formation assays showed that ARID1A-deficient cells exhibited hypersensitivity to infrared (IR) treatment, with an ∼40% slower growth rate observed in ARID1A-deficient cells (Figure 7A). Next, we found that ARID1A^{WT} but not ARID1A^{3A} rescued the IR

Figure 5. ATM-dependent recruitment of ARID1A to DSB site is required for R-loop resolution

(A) Immunofluorescence staining showing ARID1A and γH2AX signal in laser microirradiation-induced DNA damage sites in HeLa cells treated as indicated. The ARID1A density at DSB stripes was quantified by ImageJ. ***$p < 0.001$; ns, no significance.

(B and C) Immunoprecipitation analysis to determine ARID1A phosphorylation status in response to DNA damage. Cell lysates were immunoprecipitated using an anti-ARID1A antibody and analyzed by western blotting using a p-S/TQ antibody.

(D) ChIP-PCR analysis showing the binding of ARID1A to damaged DNA after ATM inhibition.

(E) Dynamics of ARID1A accumulation at DNA damage sites monitored by laser microirradiation-coupled live-cell imaging. The fluorescent intensity at DSBs was quantified with ImageJ.

(F) *In vitro* phosphorylation assay using bacterially purified His-ARID1A in the presence or absence of ATM kinase and ATP. ARID1A phosphorylation was monitored by western blotting using an anti-p-S/TQ antibody.

(G) Sequence alignment of potential ATM substrate motifs in ARID1A among different species; key residues are shown in red.

(H and I) Validation of ARID1A phosphorylation at S514/519/523 in response to DNA damage *in vivo* and *in vitro*. ARID1A phosphorylation was monitored by western blotting using a p-S/TQ motif antibody.

(J) Dynamics of WT-ARID1A and 3A-ARID1A accumulation at DNA damage sites monitored by laser microirradiation-coupled live-cell imaging.

(K–M) The S9.6 DRIP (K), m6A-DIP (L), and DRIP (S9.6)-re-DIP (m6A) (K) showing the enrichment of R-loops, m6A, and m6A-modified R-loops at DSB sites induced by 4-OHT (500 nM) in the AsiSI-U2OS system. **$p < 0.01$; ***$p < 0.001$.

(N) *In situ* PLA of the interaction between S9.6 and m6A in HeLa cells after inducing an ARID1A phosphorylation mutation. ***$p < 0.001$.

Each assay was conducted in a minimum of three independent experiments. Data represent the means ± SEM for (A) and (N) and means ± SD for (K–M). Scale bar: 10 μM for (A) and (N) and 20 μM for (E) and (J).

CellPress
OPEN ACCESS

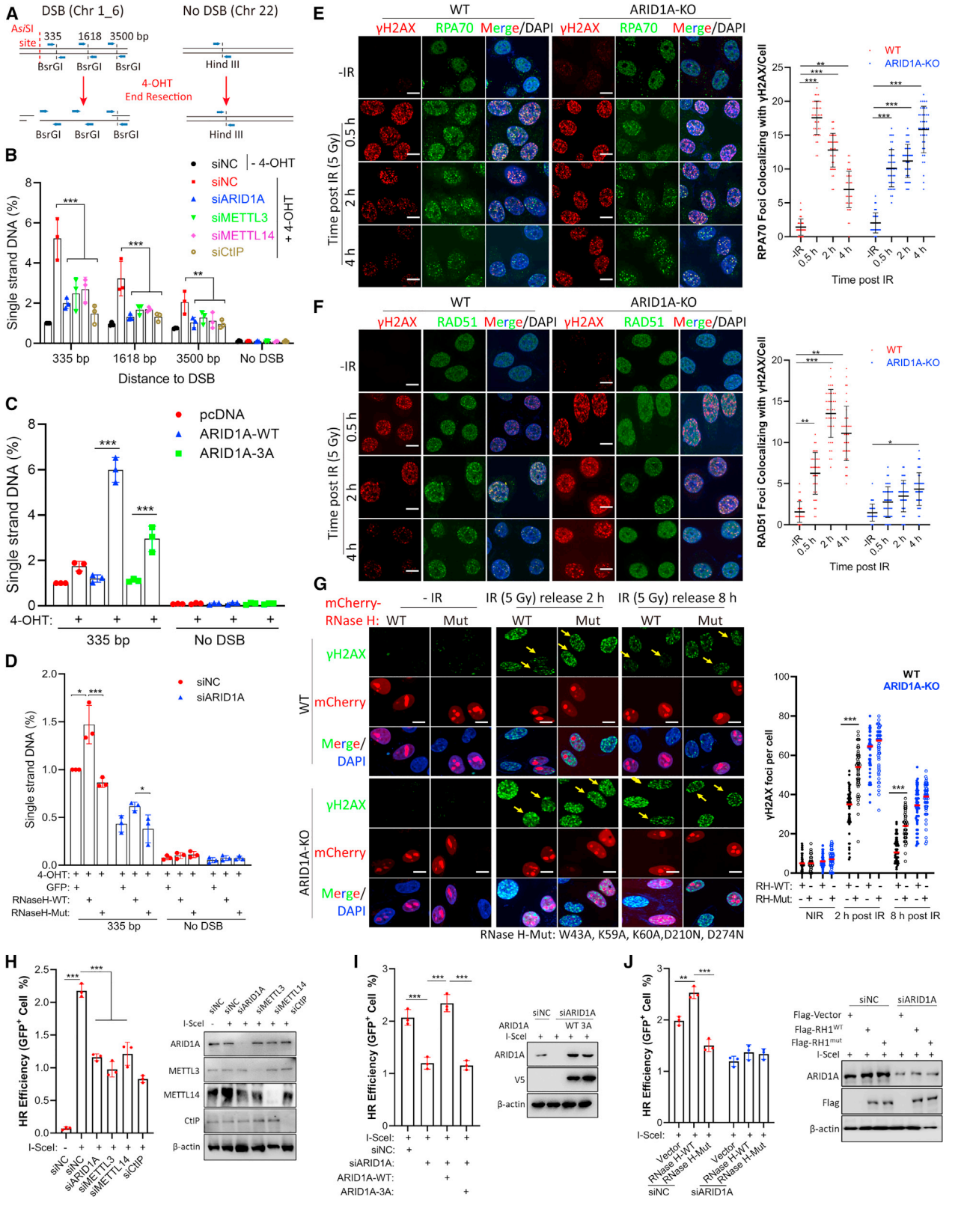

(legend on next page)

sensitivity induced by ARID1A deficiency (Figure 7B), and overexpressing a WT-RNase H1 in ARID1A-deficient cells failed to rescue the IR sensitivity (Figure 7C). We further used comet assay and observed a higher proportion of ARID1A knockout (ARID1A-KO) cells contained residual DSB lesions, as indicated by the longer tail moment 8 h after DNA damage (Figure 7D). Rescuing of $ARID1A^{WT}$ but not $ARID1A^{3A}$ in ARID1A-KO cells enhanced the DNA damage repair efficiency (Figure 7E). Moreover, by assessing the chromosomal breaks in ARID1A-deficient cells following IR treatment, we found that ARID1A deficiency abolished the repair of IR-induced chromosomal breaks, as indicated by the reduced amount of chromosome aberrations (Figures 7F and 7G). We further examined the genome aberrations (deletions and mutations) arising during the repair of A*si*SI-induced DSBs at the RBMXL1 locus, a transcriptionally active gene in the U2OS-A*si*SI-ER system. Based on a TA-cloning assay presented in the diagram, we found that the aberration sizes around the A*si*SI site were higher in ARID1A-depleted cells (quartiles ~4) than WT cells (quartiles ~1) (Figure 7H), suggesting that ARID1A deficiency impairs the DNA damage repair and genome stability maintenance.

Finally, we characterized the biological relevance of ARID1A in cancer cell resistance to DNA-damaging therapies. We assessed the clinical relevance of the ARID1A/R-loop/m6A axis in cervical cancer tissues taken from patients who had received chemo-/radiotherapies. We collected tissues from 35 clinical patients and extracted cell lysates for western blotting as R-loop signals are not stable in paraffin-embedded sections. We analyzed the intensity of ARID1A/R-loop/m6A signals in each sample (Figures 7I and 7J). ARID1A expression levels negatively correlated with R-loops (R^2 = 0.3122 and p = 0.0005) but positively correlated with m6A signals (R^2 = 0.5682 and p < 0.0001). High S9.6 levels were associated with low m6A levels (R^2 = 0.1421 and p = 0.00256) in those tissues. By analyzing the overall survival of various cancer patients who received chemotherapy using the Kaplan-Meier Plotter database (https://kmplot.com/analysis/), we found that high ARID1A expression indicated reduced overall survival in patients with breast cancer (hazard ratio = 1.58; log rank p = 0.035), ovarian cancer (hazard ratio = 1.35; log rank p < 0.001), and lung cancer (hazard ratio = 1.75; log rank p = 0.042) who received genotoxic treatment clinically (Figure 7K). Specificity, high ARID1A expression showed reduced overall survival for ovarian cancer patients who received Taxol, Platin, and Taxol plus Platin treatment (Figures S7A–S7C), as well as 5-FU-treated gastric cancer patients (Figure S7D), suggesting ARID1A has key clinical relevance in genotoxic treatment resistance. Taken together, all these observations suggest that ARID1A is a critical mediator of genome stability maintenance and cellular resistance to DNA-damaging treatment.

DISCUSSION

The precise regulation and resolution of R-loops during the DNA damage response are still not fully understood. We demonstrated that ARID1A plays a crucial role in recognizing R-loops and facilitating their resolution to maintain genome stability, by recruiting the METTL3 to local DSBs to initiate the R-loop m6A modification. In this context, m6A modification determines the fate of R-loops by efficiently recruiting RNase H1 in a timely and efficient manner during DNA damage repair (Figure 7L). Our findings suggest that patients with high levels of ARID1A exhibit resistance to genotoxic therapies. These discoveries provide avenues for exploring therapeutic strategies in cancers characterized by ARID1A abnormalities.

Several studies have reported a connection between R-loops, RNase H1, and the DNA repair machinery.[16,18,47,48] RNase H1 is recruited to DSBs to resolve R-loops in cells.[18,48] This recruitment is dependent on transcriptional activity at damaged loci, as inhibiting transcription abolishes RNase H1 recruitment.[47,49] Interestingly, studies suggest that purified RNase H1 directly binds to RPA and stimulates its enzyme activity.[22,50] Our study characterized an approach for RNase H1 recruitment via binding to m6A-methylated R-loop, which is required for R-loop resolution and DSB repair. This preferential binding of RNase H1 to m6A-modified R-loops accelerates their timely and precise clearance, thus safeguarding chromatin homeostasis. Additionally, m6A-modified R-loops have been reported to recruit other factors such as YTHDC1 and YTHDF2 to secure genomic stability.[29,51] Our data thus expand our knowledge of R-loop resolution in DNA damage repair.

Recent studies have highlighted the importance of RNA modifications in the DNA damage repair process. RNA methyltransferase TRDMT1 catalyzes the m5C modification at DSBs, promoting HR.[52,53] Although the role of m6A in R-loop biology remains poorly characterized,[54,55] it is known that METTL3 catalyzes m6A modification on RNAs involved in the DNA damage repair (DDR).[23,27,29,51] Yet contradictory findings on the impact of METTL3-mediated R-loop m6A RNA methylation on R-loop resolution have been reported. m6A modification increases R-loop accumulation and

Figure 6. ARID1A-mediated R-loop resolution facilitates end resection and DNA damage repair

(A) Schematic of the quantitative DNA resection assay based on the A*si*SI system.

(B–D) Quantitative measurement of ssDNA generation by 5′ end resection at A*si*SI-induced DSBs. A*si*SI-U_2OS cells pretreated with the indicated siRNAs were incubated with 4-OHT (500 nM) for 4 h (B) or transfected with an ARID1A dephosphorylation mimic (C) or RNase H1 enzymatic-dead mutant (D). Genomic DNA was extracted and digested with either *BsrGI* or *Hind III*. The percentage of ssDNA intermediates at the indicated sites was measured by qPCR after restriction enzyme digestion. *p < 0.05; **p < 0.01; ***p < 0.001.

(E and F) Immunofluorescence staining showing the kinetics of RPA70 (E) and RAD51 (F) foci formation and disappearance from WT and ARID1A-deficient HeLa cells exposed to 5 Gy IR. *p < 0.05; **p < 0.01; ***p < 0.001.

(G) Immunofluorescence staining showing the kinetics of γH2AX foci at different time points from WT and ARID1A-deficient HeLa cells exposed to 5 Gy IR. ***p < 0.001.

(H–J) Flow cytometric analysis of HR repair efficiency in DR-U2OS cells transfected with different siRNAs (H) or transfected with an ARID1A dephosphorylation mimic (I) or RNase H1 enzymatic-dead mutant (J) for overexpression. **p < 0.01; ***p < 0.001.

Each assay was conducted in a minimum of three independent experiments. Data represent the means ± SEM for (E–G) and means ± SD for (B–D and H–J). Scale bar: 10 μM for (A), (F), and (G).

CellPress
OPEN ACCESS

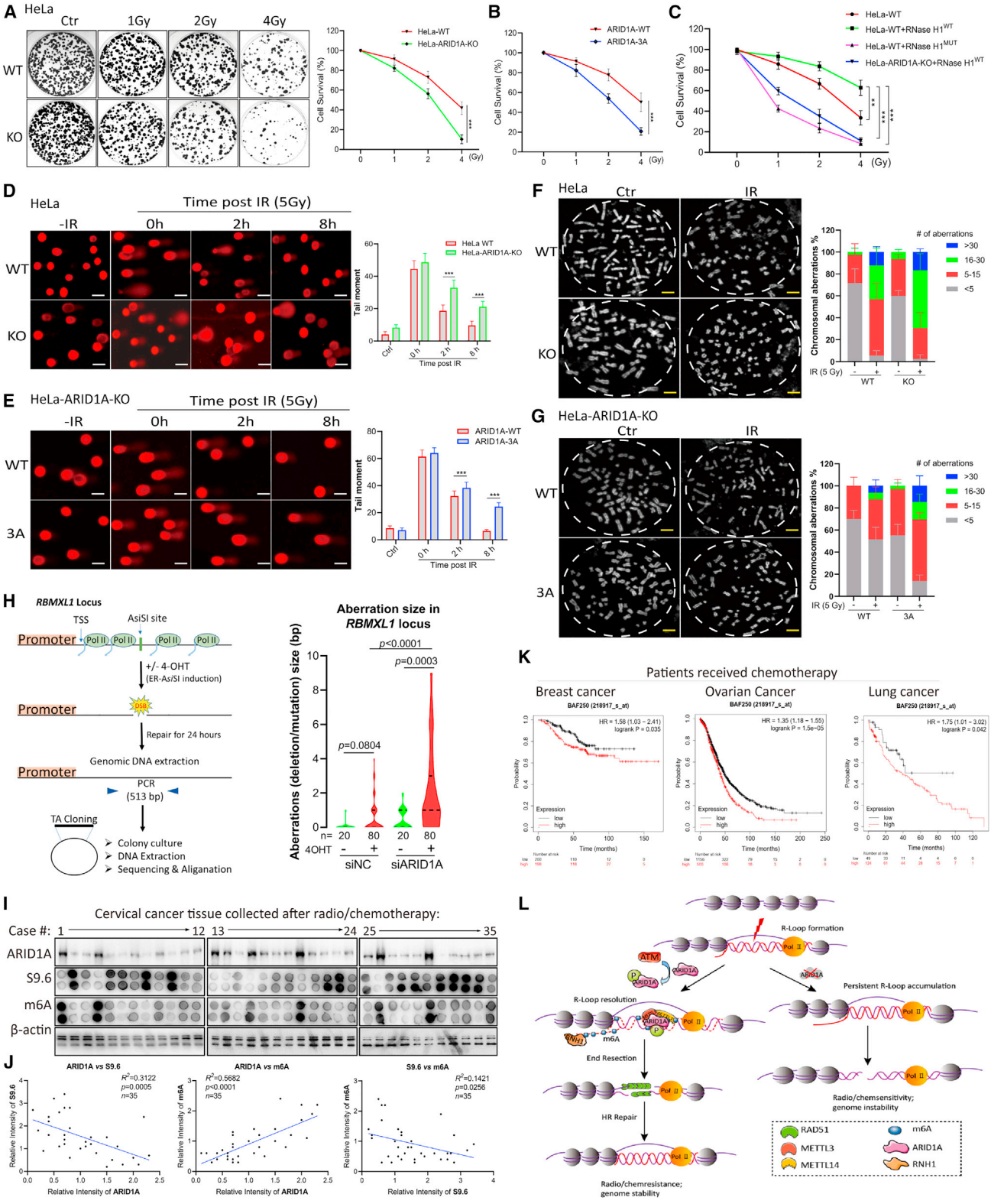

Figure 7. ARID1A is a critical mediator of genome stability maintenance and cellular resistance to DNA-damaging treatment

(A–C) Colony-formation assay showing the relative survival of different constructs co-expressed in HeLa cells irradiated with IR. The clones were analyzed by crystal violet staining, and representative images were captured using a Bio-Rad ChemiDoc XRS+. **p < 0.01; ***p < 0.001.

(legend continued on next page)

stabilization at DSBs by recruiting m6A reader YTHDC1,[29] while others suggest that it enhances the binding affinity of R-loops to YTHDC1, promoting their clearance.[23,51] We found that the ARID1A-METTL3 axis promotes R-loop m6A methylation, ultimately leading to R-loop resolution and DSB repair. These opposing observations may be context dependent and related to the different stages of R-loop generation during DNA damage. Although R-loops might have a protective role before resection,[56–59] they can interfere with RPA binding to ssDNA and must be removed after HR commitment.[16,60–63] Regardless of their nature, all R-loops generated during DNA damage need to be resolved for precise repair of damaged chromatin. Because R-loop formation and resolution are quite dynamic in a context-dependent manner,[64,65] studies aimed at dissecting the context of R-loop generation, and their intersection in the period of DSB repair, will be important to further delineate the role of R-loops in genome stability maintenance.

ARID1A helps to resolve R-loop-mediated transcription-replication conflicts to maintain genome stability.[39,66,67] Here, we identified two epigenetic regulators that are involved in RNA methylation modification, METTL3 and METTL14, which are loaded onto R-loops dynamically in an ARID1A-dependent manner. While METTL3 is recruited to chromatin to drive DSB repair through ATM-[29] or PARP1[68]-mediated post-translational modifications (PTMs), our findings suggest that ARID1A-mediated METTL3 recruitment to R-loops has pivotal roles beyond PTM-mediated recruitment. First, overexpression of METTL3 in ARID1A-deficient cells has no additive effect, implying that ARID1A's role in METTL3 recruitment extends beyond PTM. Second, the ARID1A-mediated recruitment of METTL3 specifically occurs at R-loops on DSBs rather than randomly at DSBs, indicating a more precise spatial involvement in R-loop biology. Third, ARID1A deficiency abolishes METTL3 loading, while depletion of METTL3 does not affect ARID1A's recognition of R-loops, suggesting a temporal role of ARID1A-METTL3 in R-loop regulation. Although the complexity of protein PTMs on kinase/enzymatic activity and cellular distribution is known, it is currently unclear whether the METTL3 PTMs cooperate to facilitate the DNA damage response after recruitment to R-loops by ARID1A. Therefore, further investigation is warranted to dissect the interactions between ARID1A-mediated METTL3 recruitment and its PTMs aiming to elucidate the potential coordination of METTL3 in R-loop regulation and DNA damage repair.

Loss of *ARID1A* impairs enhancer-mediated gene regulation and drives tumorigenesis,[31,69] and it potentially influences genome stability.[35,39,66,70] Our study sheds light on these observations by directly demonstrating that ARID1A recognizes the R-loop and promotes R-loop resolution in an ATM-dependent manner, thus promoting HR-mediated DNA repair. Previous data have shown that excessive R-loop accumulation at the genome threatens DNA damage repair and leads to genome instability.[39,66,67] Our data also show that loss of proximity ligation between RNase H1 and S9.6, along with reduced ARID1A binding at R-loop-prone sites, hinders the clearance of R-loops at DSB sites, ultimately leading to genome instability. Considering this, we propose that ARID1A-deficiency-driving tumorigenesis may be due, partly, to perturb R-loop clearance and chromatin homeostasis. ARID1A deficiency ultimately results in HR defects, making it a potentially effective target for many small molecules, including PARP1i,[35,36] HDAC6i,[71] EZH2i,[72] and ATM/ATRi.[73] We show that low ARID1A expression correlates with an improved response to genotoxic treatment in clinical cancer patients. This effect occurs because high ARID1A expression in these tissues leads to R-loop resolution and facilitates DNA damage repair induced by chemotherapeutics, thus reducing therapy efficacy. Therefore, the expression levels of ARID1A could be a potential biomarker for the development of combination therapy in various cancer treatments.

In conclusion, our findings show that ARID1A-METTL3-mediated m6A RNA modification occurs on R-loops, contributing to R-loop resolution to safeguard genome stability. In this context, m6A modification of R-loop RNA determines the fate of R-loops by efficiently recruiting RNase H1 in a timely and efficient manner during DNA damage repair. This ARID1A-METTL3-m6A axis in R-loop resolution and genome stability opens avenues to explore therapeutic strategies in cancers characterized by ARID1A abnormalities.

Limitations of the study

Our study characterized the role of the ARID1A-METTL3-m6A axis in regulating the R-loops stability by recruiting RNase H1 to DSB sites in response to DNA-damaging agent treatment and highlighted its potential roles in cancer chemo-/radiotherapies in clinical patients. We have described the binding of RNase H1 to m6A-modified R-loops in a high affinity

(D and E) Comet assay showing the DSB repair efficiency in WT and ARID1A-KO HeLa cells (D) or HeLa-ARID1A-KO cells stably expressing $ARID1A^{WT}$ and $ARID1A^{3A}$ (E) after 3 Gy IR for the indicated time. Relative tail moments of ≥100 cells were quantified with ImageJ. **p < 0.01; ***p < 0.001.

(F and G) Chromosome aberration analysis showing the genome stability of WT and ARID1A-KO HeLa cells (E) or WT and HeLa-ARID1A-KO cells stably expressing 3A (F) after 3 Gy IR for the indicated time. At least 50 metaphases were counted, and the results were plotted.

(H) A schematic representation of the deletion analysis at a transcriptionally active locus using A*si*SI-U_2OS cells (left). This was after DSB induction by 4-OHT (500 nM) for 4 h. The cells were left for repair, and the genomic DNA was extracted and subjected for TA cloning. The effect of ARID1A depletion on the deletions within the transcriptionally active *RBMXL1* locus at chromosome 1 was analyzed by sequencing.

(I) The expression levels of ARID1A, R-loop, and m6A from 35 cervical cancer tissues obtained from patients who received radio-/chemotherapy were analyzed by western blot/dot blot.

(J) Dot plot showing the correlation between ARID1A, R-loop, and m6A levels in different tissue samples. The correlation coefficient R^2 and the p value were obtained from linear regression analysis.

(K) Kaplan-Meier analysis of ARID1A expression and its correlation with overall survival in cancer patients who received genotoxic treatment. The hazard ratio and 95% confidence interval values are shown. In each case, the p values were obtained from the log rank test.

(L) Working model of ARID1A-METTL3-mediated R-loop m6A modification to resolve R-loop formation during the DNA damage response. Each assay was conducted in a minimum of three independent experiments. Data represent the means ± SD for (A)–(E). Scale bar: 5 μM for (D) and (E) and 20 μM for (F) and (G).

biochemically *in vitro*. However, it was still not clear how m6A-modified R-loops recognize RNase H1 structurally in a timely and efficient manner. Furthermore, since our ARID1A interactome data suggest that ARID1A interacts with the RNA methyltransferase complex in the context of DNA damage, even though we have characterized that ARID1A is required for METTL3 recruitment to DSB sites and the possible *in vivo* binding ability, it will be interesting to fully characterize the binding between ARID1A and METTL3 by mapping the possible domains based on their structure, which will provide insights into exploring therapeutic strategies in cancers by disrupting their interactions.

STAR★METHODS

Detailed methods are provided in the online version of this paper and include the following:

- KEY RESOURCES TABLE
- RESOURCE AVAILABILITY
  - Lead contact
  - Materials availability
  - Data and code availability
- EXPERIMENTAL MODEL AND STUDY PARTICIPANT DETAILS
  - Cell lines
  - Patient specimens
- METHOD DETAILS
  - Cell treatment
  - Plasmids and transfection
  - Lentivirus packaging and infection
  - Protein extraction and immunoblotting analysis
  - Immunoprecipitation
  - Proximity-dependent biotinylation identification assay (BioID)
  - Chromosome aberration assay
  - Comet assay
  - Immunofluorescent staining
  - *In situ* proximity ligation assay (PLA)
  - Laser microirradiation-coupled live-cell imaging and IR
  - S9.6 DRIP and m6A DIP
  - Isolation of chromatin fractionation RNA
  - Dot blots analysis
  - Microscale thermophoresis (MST) assay
  - Chromatin immunoprecipitation (ChIP) and qPCR analysis
  - TA colon-based deletion assay
  - Flow cytometry
  - Colony-formation assay
  - Patient specimens treatment
  - Kaplan–Meier survival analysis
- QUANTIFICATION AND STATISTICAL ANALYSIS

SUPPLEMENTAL INFORMATION

Supplemental information can be found online at https://doi.org/10.1016/j.celrep.2024.113779.

ACKNOWLEDGMENTS

This work was supported by the National Natural Science Foundation of China (32090030, 32090033, and 82002986), Guangdong Basic and Applied Basic Research Foundation (2021A1515011126), Shenzhen Municipal Commission of Science and Technology Innovation (JCYJ20200109114214463, JCYJ20220818100015032, and RCYX20210706092040047), Shenzhen Medical Research Fund (A2303025 and B2302010), Shenzhen University 2035 Program for Excellent Research, and Shenzhen University Startup Grant for Youth. The authors would like to thank Dr. Gaëlle Legube (Université Paul Sabatier, Toulouse, France) for providing the AsiSI-ER-U2OS-AID cells, Prof. Jianfeng Shen (Shanghai Jiaotong University, China) for critical discussion and suggestions, and Dr. Jessica Tamanini of ETediting, UK, for language editing.

AUTHOR CONTRIBUTIONS

Conceptualization, J.Z. and W.-G.Z.; methodology, J.Z., Z.C.L., Y.T., Q.Z., B.P., X.Y.L., and X.P.L.; investigation, J.Z., F.C., M.T., W.C.X., and Y.X.S.; writing–original draft, J.Z. and F.C.; writing–review & editing, J.Z., X.Z.X., M.G., and W.-G.Z.; funding acquisition, J.Z. and W.-G.Z.; resources, X.Y.L., X.Z.X., and M.G.; supervision, W.-G.Z.

DECLARATION OF INTERESTS

The authors declare no competing interests.

Received: July 12, 2023
Revised: December 2, 2023
Accepted: January 26, 2024
Published: February 13, 2024

REFERENCES

1. García-Muse, T., and Aguilera, A. (2019). R Loops: From Physiological to Pathological Roles. Cell *179*, 604–618. https://doi.org/10.1016/j.cell.2019.08.055.
2. Petermann, E., Lan, L., and Zou, L. (2022). Sources, resolution and physiological relevance of R-loops and RNA-DNA hybrids. Nat. Rev. Mol. Cell Biol. *23*, 521–540. https://doi.org/10.1038/s41580-022-00474-x.
3. Crossley, M.P., Bocek, M., and Cimprich, K.A. (2019). R-Loops as Cellular Regulators and Genomic Threats. Mol. Cell *73*, 398–411. https://doi.org/10.1016/j.molcel.2019.01.024.
4. Sollier, J., and Cimprich, K.A. (2015). Breaking bad: R-loops and genome integrity. Trends Cell Biol. *25*, 514–522. https://doi.org/10.1016/j.tcb.2015.05.003.
5. Skourti-Stathaki, K., and Proudfoot, N.J. (2014). A double-edged sword: R loops as threats to genome integrity and powerful regulators of gene expression. Genes Dev. *28*, 1384–1396. https://doi.org/10.1101/gad.242990.114.
6. Gorthi, A., Romero, J.C., Loranc, E., Cao, L., Lawrence, L.A., Goodale, E., Iniguez, A.B., Bernard, X., Masamsetti, V.P., Roston, S., et al. (2018). EWS-FLI1 increases transcription to cause R-loops and block BRCA1 repair in Ewing sarcoma. Nature *555*, 387–391. https://doi.org/10.1038/nature25748.
7. Bhatia, V., Barroso, S.I., García-Rubio, M.L., Tumini, E., Herrera-Moyano, E., and Aguilera, A. (2014). BRCA2 prevents R-loop accumulation and associates with TREX-2 mRNA export factor PCID2. Nature *511*, 362–365. https://doi.org/10.1038/nature13374.
8. Crow, Y.J., Leitch, A., Hayward, B.E., Garner, A., Parmar, R., Griffith, E., Ali, M., Semple, C., Aicardi, J., Babul-Hirji, R., et al. (2006). Mutations in genes encoding ribonuclease H2 subunits cause Aicardi-Goutieres syndrome and mimic congenital viral brain infection. Nat. Genet. *38*, 910–916. https://doi.org/10.1038/ng1842.

9. Groh, M., and Gromak, N. (2014). Out of balance: R-loops in human disease. PLoS Genet. *10*, e1004630. https://doi.org/10.1371/journal.pgen.1004630.

10. Moreira, M.-C., Klur, S., Watanabe, M., Németh, A.H., Le Ber, I., Moniz, J.-C., Tranchant, C., Aubourg, P., Tazir, M., Schöls, L., et al. (2004). Senataxin, the ortholog of a yeast RNA helicase, is mutant in ataxia-ocular apraxia 2. Nat. Genet. *36*, 225–227.

11. Cristini, A., Groh, M., Kristiansen, M.S., and Gromak, N. (2018). RNA/DNA Hybrid Interactome Identifies DXH9 as a Molecular Player in Transcriptional Termination and R-Loop-Associated DNA Damage. Cell Rep. *23*, 1891–1905. https://doi.org/10.1016/j.celrep.2018.04.025.

12. Song, C., Hotz-Wagenblatt, A., Voit, R., and Grummt, I. (2017). SIRT7 and the DEAD-box helicase DDX21 cooperate to resolve genomic R loops and safeguard genome stability. Genes Dev. *31*, 1370–1381. https://doi.org/10.1101/gad.300624.117.

13. Nguyen, H.D., Leong, W.Y., Li, W., Reddy, P.N.G., Sullivan, J.D., Walter, M.J., Zou, L., and Graubert, T.A. (2018). Spliceosome Mutations Induce R Loop-Associated Sensitivity to ATR Inhibition in Myelodysplastic Syndromes. Cancer Res. *78*, 5363–5374. https://doi.org/10.1158/0008-5472.CAN-17-3970.

14. Chen, L., Chen, J.-Y., Huang, Y.-J., Gu, Y., Qiu, J., Qian, H., Shao, C., Zhang, X., Hu, J., Li, H., et al. (2018). The Augmented R-Loop Is a Unifying Mechanism for Myelodysplastic Syndromes Induced by High-Risk Splicing Factor Mutations. Mol. Cell *69*, 412–425.e6. https://doi.org/10.1016/j.molcel.2017.12.029.

15. Lockhart, A., Pires, V.B., Bento, F., Kellner, V., Luke-Glaser, S., Yakoub, G., Ulrich, H.D., and Luke, B. (2019). RNase H1 and H2 Are Differentially Regulated to Process RNA-DNA Hybrids. Cell Rep. *29*, 2890–2900.e5. https://doi.org/10.1016/j.celrep.2019.10.108.

16. Amon, J.D., and Koshland, D. (2016). RNase H enables efficient repair of R-loop induced DNA damage. Elife *5*, e20533. https://doi.org/10.7554/eLife.20533.

17. Wahba, L., Amon, J.D., Koshland, D., and Vuica-Ross, M. (2011). RNase H and multiple RNA biogenesis factors cooperate to prevent RNA:DNA hybrids from generating genome instability. Mol. Cell *44*, 978–988. https://doi.org/10.1016/j.molcel.2011.10.017.

18. D'Alessandro, G., Whelan, D.R., Howard, S.M., Vitelli, V., Renaudin, X., Adamowicz, M., Iannelli, F., Jones-Weinert, C.W., Lee, M., Matti, V., et al. (2018). BRCA2 controls DNA:RNA hybrid level at DSBs by mediating RNase H2 recruitment. Nat. Commun. *9*, 5376. https://doi.org/10.1038/s41467-018-07799-2.

19. Cerritelli, S.M., and Crouch, R.J. (2009). Ribonuclease H: the enzymes in eukaryotes. FEBS J. *276*, 1494–1505. https://doi.org/10.1111/j.1742-4658.2009.06908.x.

20. Lim, Y.W., Sanz, L.A., Xu, X., Hartono, S.R., and Chédin, F. (2015). Genome-wide DNA hypomethylation and RNA:DNA hybrid accumulation in Aicardi-Goutieres syndrome. Elife *4*, e08007. https://doi.org/10.7554/eLife.08007.

21. Stirling, P.C., Chan, Y.A., Minaker, S.W., Aristizabal, M.J., Barrett, I., Sipahimalani, P., Kobor, M.S., and Hieter, P. (2012). R-loop-mediated genome instability in mRNA cleavage and polyadenylation mutants. Genes Dev. *26*, 163–175. https://doi.org/10.1101/gad.179721.111.

22. Nguyen, H.D., Yadav, T., Giri, S., Saez, B., Graubert, T.A., and Zou, L. (2017). Functions of Replication Protein A as a Sensor of R Loops and a Regulator of RNaseH1. Mol. Cell *65*, 832–847.e4. https://doi.org/10.1016/j.molcel.2017.01.029.

23. Kang, H.J., Cheon, N.Y., Park, H., Jeong, G.W., Ye, B.J., Yoo, E.J., Lee, J.H., Hur, J.H., Lee, E.A., Kim, H., et al. (2021). TonEBP recognizes R-loops and initiates m6A RNA methylation for R-loop resolution. Nucleic Acids Res. *49*, 269–284. https://doi.org/10.1093/nar/gkaa1162.

24. Zhao, B.S., Roundtree, I.A., and He, C. (2017). Post-transcriptional gene regulation by mRNA modifications. Nat. Rev. Mol. Cell Biol. *18*, 31–42. https://doi.org/10.1038/nrm.2016.132.

25. Frye, M., Harada, B.T., Behm, M., and He, C. (2018). RNA modifications modulate gene expression during development. Science *361*, 1346–1349. https://doi.org/10.1126/science.aau1646.

26. Liu, J., Yue, Y., Han, D., Wang, X., Fu, Y., Zhang, L., Jia, G., Yu, M., Lu, Z., Deng, X., et al. (2014). A METTL3-METTL14 complex mediates mammalian nuclear RNA N6-adenosine methylation. Nat. Chem. Biol. *10*, 93–95. https://doi.org/10.1038/nchembio.1432.

27. Xiang, Y., Laurent, B., Hsu, C.H., Nachtergaele, S., Lu, Z., Sheng, W., Xu, C., Chen, H., Ouyang, J., Wang, S., et al. (2017). RNA m(6)A methylation regulates the ultraviolet-induced DNA damage response. Nature *543*, 573–576. https://doi.org/10.1038/nature21671.

28. Abakir, A., Giles, T.C., Cristini, A., Foster, J.M., Dai, N., Starczak, M., Rubio-Roldan, A., Li, M., Eleftheriou, M., Crutchley, J., et al. (2020). N(6)-methyladenosine regulates the stability of RNA:DNA hybrids in human cells. Nat. Genet. *52*, 48–55. https://doi.org/10.1038/s41588-019-0549-x.

29. Zhang, C., Chen, L., Peng, D., Jiang, A., He, Y., Zeng, Y., Xie, C., Zhou, H., Luo, X., Liu, H., et al. (2020). METTL3 and N6-Methyladenosine Promote Homologous Recombination-Mediated Repair of DSBs by Modulating DNA-RNA Hybrid Accumulation. Mol. Cell *79*, 425–442.e7. https://doi.org/10.1016/j.molcel.2020.06.017.

30. Marnef, A., and Legube, G. (2020). m6A RNA modification as a new player in R-loop regulation. Nat. Genet. *52*, 27–28. https://doi.org/10.1038/s41588-019-0563-z.

31. Wilson, B.G., and Roberts, C.W.M. (2011). SWI/SNF nucleosome remodellers and cancer. Nat. Rev. Cancer *11*, 481–492. https://doi.org/10.1038/nrc3068.

32. Wu, J.N., and Roberts, C.W.M. (2013). ARID1A mutations in cancer: another epigenetic tumor suppressor? Cancer Discov. *3*, 35–43. https://doi.org/10.1158/2159-8290.CD-12-0361.

33. Mullen, J., Kato, S., Sicklick, J.K., and Kurzrock, R. (2021). Targeting ARID1A mutations in cancer. Cancer Treat Rev. *100*, 102287. https://doi.org/10.1016/j.ctrv.2021.102287.

34. Kadoch, C., Hargreaves, D.C., Hodges, C., Elias, L., Ho, L., Ranish, J., and Crabtree, G.R. (2013). Proteomic and bioinformatic analysis of mammalian SWI/SNF complexes identifies extensive roles in human malignancy. Nat. Genet. *45*, 592–601. https://doi.org/10.1038/ng.2628.

35. Park, Y., Chui, M.H., Suryo Rahmanto, Y., Yu, Z.C., Shamanna, R.A., Bellani, M.A., Gaillard, S., Ayhan, A., Viswanathan, A., Seidman, M.M., et al. (2019). Loss of ARID1A in Tumor Cells Renders Selective Vulnerability to Combined Ionizing Radiation and PARP Inhibitor Therapy. Clin. Cancer Res. *25*, 5584–5594. https://doi.org/10.1158/1078-0432.CCR-18-4222.

36. Shen, J., Peng, Y., Wei, L., Zhang, W., Yang, L., Lan, L., Kapoor, P., Ju, Z., Mo, Q., Shih, I.M., et al. (2015). ARID1A Deficiency Impairs the DNA Damage Checkpoint and Sensitizes Cells to PARP Inhibitors. Cancer Discov. *5*, 752–767. https://doi.org/10.1158/2159-8290.CD-14-0849.

37. Zhao, B., Lin, J., Rong, L., Wu, S., Deng, Z., Fatkhutdinov, N., Zundell, J., Fukumoto, T., Liu, Q., Kossenkov, A., et al. (2019). ARID1A promotes genomic stability through protecting telomere cohesion. Nat. Commun. *10*, 4067. https://doi.org/10.1038/s41467-019-12037-4.

38. Williamson, C.T., Miller, R., Pemberton, H.N., Jones, S.E., Campbell, J., Konde, A., Badham, N., Rafiq, R., Brough, R., Gulati, A., et al. (2016). ATR inhibitors as a synthetic lethal therapy for tumours deficient in ARID1A. Nat. Commun. *7*, 13837. https://doi.org/10.1038/ncomms13837.

39. Tsai, S., Fournier, L.-A., Chang, E.Y.-C., Wells, J.P., Minaker, S.W., Zhu, Y.D., Wang, A.Y.-H., Wang, Y., Huntsman, D.G., and Stirling, P.C. (2021). ARID1A regulates R-loop associated DNA replication stress. PLoS Genet. *17*, e1009238. https://doi.org/10.1371/journal.pgen.1009238.

40. Watanabe, R., Ui, A., Kanno, S.-I., Ogiwara, H., Nagase, T., Kohno, T., and Yasui, A. (2014). SWI/SNF factors required for cellular resistance to DNA damage include ARID1A and ARID1B and show interdependent protein stability. Cancer Res. *74*, 2465–2475. https://doi.org/10.1158/0008-5472.CAN-13-3608.

41. Ji, L., and Chen, X. (2012). Regulation of small RNA stability: methylation and beyond. Cell Res. *22*, 624–636. https://doi.org/10.1038/cr.2012.36.

42. Boo, S.H., and Kim, Y.K. (2020). The emerging role of RNA modifications in the regulation of mRNA stability. Exp. Mol. Med. *52*, 400–408. https://doi.org/10.1038/s12276-020-0407-z.

43. Roux, K.J., Kim, D.I., Raida, M., and Burke, B. (2012). A promiscuous biotin ligase fusion protein identifies proximal and interacting proteins in mammalian cells. J. Cell Biol. *196*, 801–810. https://doi.org/10.1083/jcb.201112098.

44. Li, X., Zhou, J., Zhao, W., Wen, Q., Wang, W., Peng, H., Gao, Y., Bouchonville, K.J., Offer, S.M., Chan, K., et al. (2022). Defining Proximity Proteomics of Histone Modifications by Antibody-mediated Protein A-APEX2 Labeling. Dev. Reprod. Biol. *20*, 87–100. https://doi.org/10.1016/j.gpb.2021.09.003.

45. Zhou, Y., Caron, P., Legube, G., and Paull, T.T. (2014). Quantitation of DNA double-strand break resection intermediates in human cells. Nucleic Acids Res. *42*, e19. https://doi.org/10.1093/nar/gkt1309.

46. Clouaire, T., Rocher, V., Lashgari, A., Arnould, C., Aguirrebengoa, M., Biernacka, A., Skrzypczak, M., Aymard, F., Fongang, B., Dojer, N., et al. (2018). Comprehensive Mapping of Histone Modifications at DNA Double-Strand Breaks Deciphers Repair Pathway Chromatin Signatures. Mol. Cell *72*, 250–262.e6. https://doi.org/10.1016/j.molcel.2018.08.020.

47. Ohle, C., Tesorero, R., Schermann, G., Dobrev, N., Sinning, I., and Fischer, T. (2016). Transient RNA-DNA Hybrids Are Required for Efficient Double-Strand Break Repair. Cell *167*, 1001–1013.e7. https://doi.org/10.1016/j.cell.2016.10.001.

48. Zhao, H., Zhu, M., Limbo, O., and Russell, P. (2018). RNase H eliminates R-loops that disrupt DNA replication but is nonessential for efficient DSB repair. EMBO Rep. *19*, e45335. https://doi.org/10.15252/embr.201745335.

49. Britton, S., Dernoncourt, E., Delteil, C., Froment, C., Schiltz, O., Salles, B., Frit, P., and Calsou, P. (2014). DNA damage triggers SAF-A and RNA biogenesis factors exclusion from chromatin coupled to R-loops removal. Nucleic Acids Res. *42*, 9047–9062. https://doi.org/10.1093/nar/gku601.

50. Petzold, C., Marceau, A.H., Miller, K.H., Marqusee, S., and Keck, J.L. (2015). Interaction with Single-stranded DNA-binding Protein Stimulates Escherichia coli Ribonuclease HI Enzymatic Activity. J. Biol. Chem. *290*, 14626–14636. https://doi.org/10.1074/jbc.M115.655134.

51. Abakir, A., Giles, T.C., Cristini, A., Foster, J.M., Dai, N., Starczak, M., Rubio-Roldan, A., Li, M., Eleftheriou, M., Crutchley, J., et al. (2020). N-methyladenosine regulates the stability of RNA:DNA hybrids in human cells. Nat. Genet. *52*, 48–55. https://doi.org/10.1038/s41588-019-0549-x.

52. Chen, H., Yang, H., Zhu, X., Yadav, T., Ouyang, J., Truesdell, S.S., Tan, J., Wang, Y., Duan, M., Wei, L., et al. (2020). m(5)C modification of mRNA serves a DNA damage code to promote homologous recombination. Nat. Commun. *11*, 2834. https://doi.org/10.1038/s41467-020-16722-7.

53. Yang, H., Wang, Y., Xiang, Y., Yadav, T., Ouyang, J., Phoon, L., Zhu, X., Shi, Y., Zou, L., and Lan, L. (2022). FMRP promotes transcription-coupled homologous recombination via facilitating TET1-mediated m5C RNA modification demethylation. Proc. Natl. Acad. Sci. USA *119*, e2116251119. https://doi.org/10.1073/pnas.2116251119.

54. Meyer, K.D., Saletore, Y., Zumbo, P., Elemento, O., Mason, C.E., and Jaffrey, S.R. (2012). Comprehensive analysis of mRNA methylation reveals enrichment in 3' UTRs and near stop codons. Cell *149*, 1635–1646. https://doi.org/10.1016/j.cell.2012.05.003.

55. Zaccara, S., Ries, R.J., and Jaffrey, S.R. (2019). Reading, writing and erasing mRNA methylation. Nat. Rev. Mol. Cell Biol. *20*, 608–624. https://doi.org/10.1038/s41580-019-0168-5.

56. Aguilera, A., and Gómez-González, B. (2017). DNA-RNA hybrids: the risks of DNA breakage during transcription. Nat. Struct. Mol. Biol. *24*, 439–443. https://doi.org/10.1038/nsmb.3395.

57. Arora, R., Lee, Y., Wischnewski, H., Brun, C.M., Schwarz, T., and Azzalin, C.M. (2014). RNaseH1 regulates TERRA-telomeric DNA hybrids and telomere maintenance in ALT tumour cells. Nat. Commun. *5*, 5220. https://doi.org/10.1038/ncomms6220.

58. Yadav, T., Zhang, J.-M., Ouyang, J., Leung, W., Simoneau, A., and Zou, L. (2022). TERRA and RAD51AP1 promote alternative lengthening of telomeres through an R- to D-loop switch. Mol. Cell *82*, 3985–4000.e4. https://doi.org/10.1016/j.molcel.2022.09.026.

59. Kaminski, N., Wondisford, A.R., Kwon, Y., Lynskey, M.L., Bhargava, R., Barroso-González, J., García-Expósito, L., He, B., Xu, M., Mellacheruvu, D., et al. (2022). RAD51AP1 regulates ALT-HDR through chromatin-directed homeostasis of TERRA. Mol. Cell *82*, 4001–4017.e7. https://doi.org/10.1016/j.molcel.2022.09.025.

60. Li, L., Germain, D.R., Poon, H.Y., Hildebrandt, M.R., Monckton, E.A., McDonald, D., Hendzel, M.J., and Godbout, R. (2016). DEAD Box 1 Facilitates Removal of RNA and Homologous Recombination at DNA Double-Strand Breaks. Mol. Cell Biol. *36*, 2794–2810. https://doi.org/10.1128/MCB.00415-16.

61. Cohen, S., Puget, N., Lin, Y.L., Clouaire, T., Aguirrebengoa, M., Rocher, V., Pasero, P., Canitrot, Y., and Legube, G. (2018). Senataxin resolves RNA:DNA hybrids forming at DNA double-strand breaks to prevent translocations. Nat. Commun. *9*, 533. https://doi.org/10.1038/s41467-018-02894-w.

62. Costantino, L., and Koshland, D. (2015). The Yin and Yang of R-loop biology. Curr. Opin. Cell Biol. *34*, 39–45. https://doi.org/10.1016/j.ceb.2015.04.008.

63. Marnef, A., and Legube, G. (2021). R-loops as Janus-faced modulators of DNA repair. Nat. Cell Biol. *23*, 305–313. https://doi.org/10.1038/s41556-021-00663-4.

64. Cristini, A., Ricci, G., Britton, S., Salimbeni, S., Huang, S.Y.N., Marinello, J., Calsou, P., Pommier, Y., Favre, G., Capranico, G., et al. (2019). Dual Processing of R-Loops and Topoisomerase I Induces Transcription-Dependent DNA Double-Strand Breaks. Cell Rep. *28*, 3167–3181.e6. https://doi.org/10.1016/j.celrep.2019.08.041.

65. Saha, S., Yang, X., Huang, S.-Y.N., Agama, K., Baechler, S.A., Sun, Y., Zhang, H., Saha, L.K., Su, S., Jenkins, L.M., et al. (2022). Resolution of R-loops by topoisomerase III-β (TOP3B) in coordination with the DEAD-box helicase DDX5. Cell Rep. *40*, 111067. https://doi.org/10.1016/j.celrep.2022.111067.

66. Bayona-Feliu, A., Barroso, S., Muñoz, S., and Aguilera, A. (2021). The SWI/SNF chromatin remodeling complex helps resolve R-loop-mediated transcription–replication conflicts. Nat. Genet. *53*, 1050–1063. https://doi.org/10.1038/s41588-021-00867-2.

67. Davó-Martínez, C., Helfricht, A., Ribeiro-Silva, C., Raams, A., Tresini, M., Uruci, S., van Cappellen, W.A., Taneja, N., Demmers, J.A.A., Pines, A., et al. (2023). Different SWI/SNF complexes coordinately promote R-loop- and RAD52-dependent transcription-coupled homologous recombination. Nucleic Acids Res. *51*, 9055–9074. https://doi.org/10.1093/nar/gkad609.

68. Xiang, Y., Laurent, B., Hsu, C.-H., Nachtergaele, S., Lu, Z., Sheng, W., Xu, C., Chen, H., Ouyang, J., Wang, S., et al. (2017). RNA mA methylation regulates the ultraviolet-induced DNA damage response. Nature *543*, 573–576. https://doi.org/10.1038/nature21671.

69. Jones, S., Wang, T.L., Shih, I.M., Mao, T.L., Nakayama, K., Roden, R., Glas, R., Slamon, D., Diaz, L.A., Jr., Vogelstein, B., et al. (2010). Frequent mutations of chromatin remodeling gene ARID1A in ovarian clear cell carcinoma. Science *330*, 228–231. https://doi.org/10.1126/science.1196333.

70. Dykhuizen, E.C., Hargreaves, D.C., Miller, E.L., Cui, K., Korshunov, A., Kool, M., Pfister, S., Cho, Y.J., Zhao, K., and Crabtree, G.R. (2013). BAF complexes facilitate decatenation of DNA by topoisomerase IIalpha. Nature *497*, 624–627. https://doi.org/10.1038/nature12146.

71. Bitler, B.G., Wu, S., Park, P.H., Hai, Y., Aird, K.M., Wang, Y., Zhai, Y., Kossenkov, A.V., Vara-Ailor, A., Rauscher, F.J., III., et al. (2017). ARID1A-mutated ovarian cancers depend on HDAC6 activity. Nat. Cell Biol. *19*, 962–973. https://doi.org/10.1038/ncb3582.

72. Bitler, B.G., Aird, K.M., Garipov, A., Li, H., Amatangelo, M., Kossenkov, A.V., Schultz, D.C., Liu, Q., Shih, I.M., Conejo-Garcia, J.R., et al. (2015). Synthetic lethality by targeting EZH2 methyltransferase activity in ARID1A-mutated cancers. Nat. Med. *21*, 231–238. https://doi.org/10.1038/nm.3799.

73. Wang, L., Yang, L., Wang, C., Zhao, W., Ju, Z., Zhang, W., Shen, J., Peng, Y., An, C., Luu, Y.T., et al. (2020). Inhibition of the ATM/Chk2 axis promotes cGAS/STING signaling in ARID1A-deficient tumors. J. Clin. Invest. *130*, 5951–5966. https://doi.org/10.1172/JCI130445.

74. Hou, T., Cao, Z., Zhang, J., Tang, M., Tian, Y., Li, Y., Lu, X., Chen, Y., Wang, H., Wei, F.Z., et al. (2020). SIRT6 coordinates with CHD4 to promote chromatin relaxation and DNA repair. Nucleic Acids Res. *48*, 2982–3000. https://doi.org/10.1093/nar/gkaa006.

75. Aymard, F., Bugler, B., Schmidt, C.K., Guillou, E., Caron, P., Briois, S., Iacovoni, J.S., Daburon, V., Miller, K.M., Jackson, S.P., and Legube, G. (2014). Transcriptionally active chromatin recruits homologous recombination at DNA double-strand breaks. Nat. Struct. Mol. Biol. *21*, 366–374. https://doi.org/10.1038/nsmb.2796.

76. Zhang, J., Jia, L., Liu, T., Yip, Y.L., Tang, W.C., Lin, W., Deng, W., Lo, K.W., You, C., Lung, M.L., et al. (2019 Jun). mTORC2-mediated PDHE1α nuclear translocation links EBV-LMP1 reprogrammed glucose metabolism to cancer metastasis in nasopharyngeal carcinoma. Oncogene *38*, 4669–4684.

77. Sanjana, N.E., Shalem, O., and Zhang, F. (2014). Improved vectors and genome-wide libraries for CRISPR screening. Nat. Methods *11*, 783–784. https://doi.org/10.1038/nmeth.3047.

78. Zhang, J., Chen, F., Tian, Y., Xu, W., Zhu, Q., Li, Z., Qiu, L., Lu, X., Peng, B., Liu, X., et al. (2023). PARylated PDHE1α generates acetyl-CoA for local chromatin acetylation and DNA damage repair. Nat. Struct. Mol. Biol. *30*, 1719–1734. https://doi.org/10.1038/s41594-023-01107-3.

79. Li, Z., Xu, W., Chen, F., Zhang, J., and Zhu, W.-G. (2024). BET inhibitors enhance the anti-cancer effect of etoposide by suppressing the MRN-ATM axis in the DNA damage response. Genes Dis. *11*, 19–22. https://doi.org/10.1016/j.gendis.2022.12.001.

80. Liao, W., McNutt, M.A., and Zhu, W.G. (2009). The comet assay: a sensitive method for detecting DNA damage in individual cells. Methods *48*, 46–53. https://doi.org/10.1016/j.ymeth.2009.02.016.

81. Alagia, A., Ketley, R.F., and Gullerova, M. (2022). Proximity Ligation Assay for Detection of R-Loop Complexes upon DNA Damage. Methods Mol. Biol. *2528*, 289–303. https://doi.org/10.1007/978-1-0716-2477-7_19.

82. Qiu, L., Xu, W., Lu, X., Chen, F., Chen, Y., Tian, Y., Zhu, Q., Liu, X., Wang, Y., Pei, X.-H., et al. (2023). The HDAC6-RNF168 axis regulates H2A/H2A.X ubiquitination to enable double-strand break repair. Nucleic Acids Res. *51*, 9166–9182. https://doi.org/10.1093/nar/gkad631.

83. Conrad, T., and Ørom, U.A. (2017). Cellular Fractionation and Isolation of Chromatin-Associated RNA. In Enhancer RNAs: Methods and Protocols, U.A. Ørom, ed. (Springer New York), pp. 1–9. https://doi.org/10.1007/978-1-4939-4035-6_1.

84. Nelson, J.D., Denisenko, O., and Bomsztyk, K. (2006). Protocol for the fast chromatin immunoprecipitation (ChIP) method. Nat. Protoc. *1*, 179–185.

STAR★METHODS

KEY RESOURCES TABLE

REAGENT or RESOURCE	SOURCE	IDENTIFIER
Antibodies		
Biotin	SANTA CRUZ	Cat.# sc-53179
RAD51	SANTA CRUZ	Cat.# sc-398587
γH2AX	Cell Signaling Technology	Cat.# 9718S
γH2AX	Cell Signaling Technology	Cat.# 80312S
ARID1A	Cell Signaling Technology	Cat.# 12354S
ARID1A	SANTA CRUZ	Cat.# sc-32761
m6A	Synaptic Systems	Cat.# 202003
m5C	Abcam	Cat.# ab10805
m7G	MBL International	Cat.# RN016M
Rabbit (DA1E) mAb IgG	Cell Signaling Technology	Cat.# 3900S
H3	ProteinTech	Cat.# 17168-1-AP
H4	ProteinTech	Cat.# 16047-1-AP
AARS1	ProteinTech	Cat.# 67909-1-Ig
β-actin	ProteinTech	Cat.# 66009-1-1g
METTL3	ProteinTech	Cat.# 67733-1-Ig
METTL3	ABclonal	Cat.# AB370
DDX21	ABclonal	Cat.# A4277
METTL14	ProteinTech	Cat.# 26158-1-AP
RNH1	ProteinTech	Cat.# 66028-1-Ig
NAT10	ProteinTech	Cat.# 67465-1-Ig
S9.6	Millipore	Cat.# MABE1095
HA	MBL	Cat.#M180-3
Flag	MBL	Cat.# pm020
Flag	Sigma-Aldrich	Cat.#F1804
V5-Tag	R&DMAB8926	Cat.# MAB8926
VeriBlot for IP Detection	abcam	Cat.# ab131366
UHRF1	Cell Signaling Technology	Cat.# 12378S
P-S/TQ	Cell Signaling Technology	Cat.# 5883S
pATM-Ser1981	Cell Signaling Technology	Cat.# MAB3082(M)
RPA70	Cell Signaling Technology	Cat.# 2267S
Anti-FLAG M2 agarose beads	Biomake	Cat.#B23102
HRP-conjugated anti-rabbit IgG antibody	Zhongshan Jinqiao	Cat.# ZB-2301
HRP-conjugated anti-mouse IgG antibody	Zhongshan Jinqiao	Cat.# ZB-2305
Alexa Fluor 488 goat anti-Rabbit	Life Technologies	Cat.# A11034
Alexa Fluor 488 goat anti-Mouse	Life Technologies	Cat.# A11029
Alexa Fluor 555 goat anti-Rabbit	Life Technologies	Cat.# A27039
Alexa Fluor 555 goat anti-Mouse	Life Technologies	Cat.# A28180
Alexa Fluor 647 goat anti-Rabbit	Life Technologies	Cat.# A32733
Alexa Fluor 647 goat anti-Mouse	Life Technologies	Cat.# A32728
Bacterial and virus strains		
Trans DH5α	TransGen Biotech	Cat.#CD201-01
Trans BL21(DE3)	TransGen Biotech	Cat.#CD601-02

(*Continued on next page*)

Continued

REAGENT or RESOURCE	SOURCE	IDENTIFIER
Biological samples		
Human cervical cancer samples received with chemo/radio-therapies	Affiliated Hospital of Shenzhen University	N/A
Chemicals, peptides, and recombinant proteins		
UltraFection 3.0	4A Biotech	Cat.# FXP135-020
Camptothecin	Medchemexpress	Cat.# HY-16560
Methylene blue	Medchemexpress	Cat.# HY-14536
G418	InvivoGen	Cat.# Ant-gn-1
Puromycin	InvivoGen	Cat.# Ant-pr-1
HindIII	Thermo Scientific™	Cat.# FD0504
BsrGI	Thermo Scientific™	Cat.# ER0932
RNase H1	Thermo Scientific™	Cat.# EN0201
RNase III	Thermo Scientific™	Cat.# AM2290
INTERFERin® transfection reagent	Polyplus	Cat.# 409-10
Etoposide	Sigma-Aldrich	Cat.#E1383-100MG
In situ Proximity Ligation Assay	Sigma-Aldrich	Cat.# DUO92002
Nicotinamide	Sigma-Aldrich	Cat.# 72340
Polybrene	Sigma-Aldrich	Cat.# TR-1003-G
Dimethyl Sulfoxide (DMSO)	MP Biomedicals	Cat.# 219141880
MMS	Selleckchem	Cat.#E0609
4-Hydroxytamoxifen (4-OHT)	Selleckchem	Cat.#S7827
KU55933	Selleckchem	Cat.#S1092
Nu-6027	Selleckchem	Cat.#S7114
UNC0638	Selleckchem	Cat.#S8071
VE-821	Selleckchem	Cat.#S8007
Olaparib	Selleckchem	Cat.#S1060
Trichostatin A	Selleckchem	Cat.#S1045
TBB	Selleckchem	Cat.#S5265
ATP	Selleckchem	Cat.#S5260
DAPI	Solarbio	Cat.#C0065
Mut Express II Fast Mutagenesis Kit	Vazyme Biotech	Cat.#C214
ClonExpress®II One Step Cloning Kit	Vazyme Biotech	Cat.#C112
2x SYBR Green qPCR Master Mix	Bimake	Cat.#B21203
Comet Assay Kit 96 Samples	Trevigen	Cat.# 4253-096-K
Protein A-Sepharose CL-4B 1.5G	Cytiva	Cat.# 17078001
Protein G-Sepharose 4 FF, 5 ML	Cytiva	Cat.# 17061801
Experimental models: Cell lines		
HeLa	ATCC	Cat.# CCL-2
HCT116	ATCC	Cat.# CCL-247
HEK293T	ATCC	Cat.# CRL-11268
EJ5-U2OS	Hou et al.[74]	PMID: 31970415
DR-U2OS	Hou et al.[74]	PMID: 31970415
AsiSI-ER-U2OS-AID	Aymard et al.[75]	PMID: 24658350
Oligonucleotides		
Human ARID1A-sgRNA #1: CACCGAGCAACAGCAGAATTACAAG	This manuscript	N/A
Human ARID1A-sgRNA #2: CACCGCAGCAGAACTCTCACGACCA	This manuscript	N/A
Human ARID1A-sgRNA #3: CACCGCCATGGCCAACAATTCTGCA	This manuscript	N/A

(*Continued on next page*)

Continued

REAGENT or RESOURCE	SOURCE	IDENTIFIER
Primers sequence for siRNAs are provided in Table S1	This manuscript	N/A
Primers sequence for qPCR analysis are provided in Table S2	This manuscript	N/A
Primers sequence for *in vitro* R-Loop makeup are provided in Table S3	This manuscript	N/A
Recombinant DNA		
I-SceI	Hou et al.[74]	PMID: 31970415
p3×Flag-CMV-10	Hou et al.[74]	PMID: 31970415
pcDNA3.1-3HA	Zhang et al.[76]	PMID: 30745576
pET-28a	Addgene	Cat.# 69864-3
PGEX-4T-1	Addgene	Cat.# 27458001
pEGFP-C1	Clontech	Cat.# 6084-1
psPAX2	Addgene	Cat.# 12260
PMD2.G	Addgene	Cat.# 12259
LentiCRISPR V2	Addgene	Cat.# 52961
BirA-ARID1A	This manuscript	Cat.# 124814
mCherry-RNaseH1^{D209N}	This manuscript	N/A
GFP-ARID1A	This manuscript	N/A
GFP-ARID1A-3A	This manuscript	N/A
GFP-METTL3	This manuscript	N/A
GFP-METTL3-APPA	This manuscript	N/A
GFP-RNaseH1	This manuscript	N/A
HIS-ARID1A	This manuscript	N/A
HIS-ARID1A-3A	This manuscript	N/A
HIS-ARID1A-1-595	This manuscript	N/A
HIS-ARID1A-591-1190	This manuscript	N/A
HIS-ARID1A-1191-1758	This manuscript	N/A
HIS-ARID1A-1-1758	This manuscript	N/A
HIS-ARID1A-1759-2285	This manuscript	N/A
Flag-METTL3	This manuscript	N/A
Flag-METTL14	This manuscript	N/A
GST-METTL3	This manuscript	N/A
pcDNA6-ARID1A	addgene	Cat.# 39311
pcDNA6-ARID1A-1-1758	addgene	Cat.# 39475
pcDNA6-ARID1A-1759-2285	addgene	Cat.# 39476
pcDNA6-ARID1A-3A	This manuscript	N/A
Flag-ATM	This manuscript	N/A
Flag-ATM-K3016R	This manuscript	N/A
Flag-ATM-K3016Q	This manuscript	N/A
Software and algorithms		
ImageJ	NIH	https://imagej.nih.gov/ij/
Cytoscape (v.3.5.1)	NIH	https://www.cytoscape.org/
BioRad ChemiDoc XRS^{+}	BioRad	https://www.bio-rad.com/
NIS ELEMENTS	Nikon	https://www.microscope.healthcare.nikon.com/
GraphPad Prism 8	Graphpad	https://www.graphpad.com/scientific-software/prism/
Adobe Illustrator CS6	Adobe	https://www.adobe.com/

(*Continued on next page*)

Continued

REAGENT or RESOURCE	SOURCE	IDENTIFIER
STRAP	Institut für Biochemie, Charité Berlin	http://www.bioinformatics.org/strap/index2.html

RESOURCE AVAILABILITY

Lead contact

Correspondence and requests for materials should be addressed to and will be fulfilled by the lead contact, Wei-Guo Zhu (zhuweiguo@szu.edu.cn).

Materials availability

Plasmids and cell lines generated in this study are available without restrictions and will be fulfilled by the lead contact upon request. Antibodies and reagents were procured from commercial sources as detailed in the key resources table.

Data and code availability

- All data in this paper will be available from the lead contact upon request.
- This paper does not report original code.
- Any additional information required is available from the lead contact upon request.

EXPERIMENTAL MODEL AND STUDY PARTICIPANT DETAILS

Cell lines

HeLa, HCT116, U2OS and human embryonic kidney (HEK) 293T cells were obtained from the American Type Culture Collection (USA) and cultured in Dulbecco's modified Eagle's medium (M&C Gene Technology, China) supplemented with 10% fetal bovine serum (FBS; Gibco, USA) and 1% penicillin/streptomycin antibiotics (M&C Gene Technology, China). A*si*SI-ER-U2OS-AID cells were obtained from Dr Gaëlle Legube (Université Paul Sabatier, Toulouse, France) and cultured in DMEM supplemented with 10% FBS and 500 μg/mL G418.[75] The two DSB repair reporter cell lines (EJ5-U2OS, DR-U2OS) were obtained from Professor Xingzhi Xu (Shenzhen University, Shenzhen, China) and cultured in DMEM supplemented with 10% FBS.[74] ARID1A-KO cells used in this study were generated using the CRISPR-Cas9 gene targeting approach, in which the cells were infected with the gRNA-harbored lentivirus and single clones were selected with puromycin (2 μg/mL). All cell lines were maintained in a humidified incubator at 37°C under 5% CO_2.

Patient specimens

A total of 35 human cervical cancer samples (female, aged 32–69 years and the average age is 49 years) were obtained from clinical patients who were diagnosed and received with chemo/radio-therapies. Studies using human specimens were approved by the Clinical Research Ethics Committee of Shenzhen University. The patients provided signed informed consent forms acknowledging the use of their resected tissues for research purposes.

METHOD DETAILS

Cell treatment

For A*si*SI-dependent DSB induction, the A*si*SI-ER-U2OS-AID cells were treated with 500 nM 4-OHT for 4 h, wherein DSBs are induced at AsiSI-target sequences across the human genome. For DSB induction by chemicals, cells were treated with 10 μM CPT or 2 mM MMS for 1 h or as mentioned specificity. For inhibitors treatment, cells were pretreated with inhibitors for 1 h before DSB induction. Chemicals concentration used for cell treatment are listed below: ATMi (KU-55933, 10 μM), ATRi (VE-821, 10 μM), PARP1i (Olaparib, 2 μM), CK2i (TBB, 50 μM), G9ai (UNC0638, 100 μM), GLPi (Bix-01294, 10 μM), PKAi (H-89, 10 μM), HDACsi (TSA, 100 nM and NAM, 100 μM).

Plasmids and transfection

The I-SceI expression construct was a gift from Prof. Xingzhi Xu. The V5-tagged ARID1A construct was obtained from Addgene. METTL3 and 14 full-length genes or fragments were amplified by PCR from cDNA (amplified from HEK293T mRNA) and cloned into 3×Flag-CMV-10, pEGFP-C1, or pET-28b vectors. All mutant constructs were generated with a Mut Express II Fast Mutagenesis Kit (Vazyme Biotech Co., Nanjing, China) based on their WT construct as the template, according to the manufacturer's protocols. All gRNAs were cloned into a LentiCRISPR-V2 vector according to the manufacturer's protocols[77]; the sequences are listed in key resources table. Plasmids were introduced into target cells using UltraFection 3.0 reagent (4A Biotech) according to the manufacturer's instructions, and all siRNAs were transfected into the target cells using INTERFERin *in vitro* siRNA/miRNA transfection reagent (Polyplus).

Lentivirus packaging and infection

Lentiviral particles were produced by transiently co-transfecting HEK293T cells with the lentiviral-based expression constructs and packaging plasmids psPAX2 and pMD2.G at a ratio of 4:3:1 using UltraFection 3.0 reagent. The viral supernatants were collected and filtered using a 0.45 μm filter (Millipore) 48 h after transfection. The virus was stored at −80°C and used to infect recipient cell lines in the presence of 8 μg/mL polybrene (Sigma).

Protein extraction and immunoblotting analysis

For whole cell protein extraction, equal numbers of cells were scraped into PBS, pelleted, and lysed in RIPA buffer (50 mM Tris-HCl, pH 8.0, 150 mM NaCl, 1% Triton X-100, 1% sodium deoxycholate, 0.1% SDS, and 1 mM EDTA) supplemented with proteinase inhibitors (Sigma) on ice for 15 min. After the addition of an equal volume of 2× sample buffer (950 μL of Laemmli buffer +50 μL β-mercaptoethanol), the lysates were then boiled for 10 min at 99°C. For chromatin fraction isolation, cells were harvested and washed in PBS by centrifugation at 1,000 ×*g* for 5 min at 4°C. The cell pellet was resuspended in 500 μL buffer I (150 mM NaCl, 50 mM HEPES [pH 7.5], 1 mM EDTA, 0.1% Triton X-100) with proteinase inhibitors and incubated for 3 min on ice before centrifugation at 13,000 ×*g* at 4°C for 3 min. The detergent-extractable supernatant was collected as the Dt fraction. The insoluble pellet was washed twice in buffer I without Triton X-100 and centrifuged at 13,000 ×*g* for 3 min at 4°C. Then, the remaining pellet containing the chromatin sample was resuspended in SDS loading buffer as the chromatin fraction, and the samples were boiled at 99°C for 10 min. For western blot analysis, the boiled samples were separated by SDS-PAGE, transferred to nitrocellulose membranes (Millipore), and incubated with the indicated primary and secondary antibodies. For the dot blot assay, the freshly prepared samples were spotted to the PVDF membrane (Millipore) after treatment with DNase I or RNase H, the membranes were activated and blocked with 3% BSA, followed by incubation with associated antibodies.

Immunoprecipitation

For immunoprecipitation experiments, cells were scraped into PBS and pelleted, and the cell pellet was resuspended in lysis buffer (20 mM Tris-HCl pH 8.0, 137 mM NaCl, 10% glycerol, 1% NP-40, 2 mM EDTA with a protease inhibitor cocktail). For the denaturing immunoprecipitation, the cells were lysed with RIPA denaturing buffer (50 mM Tris-HCl [pH 8.0], 5 mM EDTA, 150 mM NaCl, 0.5% Nonidet P-40, 0.5% deoxycholate, 0.5% SDS). After sonication, the samples were centrifuged at 13,000 ×*g* for 10 min at 4°C. The supernatant was then collected and incubated with primary antibodies or normal IgG overnight at 4°C. Protein A or Protein G Sepharose beads were added to the samples and incubated for 2 h at 4°C. The beads were then washed with lysis buffer, and the eluate was subjected to western blotting after boiling with SDS loading buffer.

For the R-Loop-associated Biotin pulldown assay, the biotin-conjugated m6A-modified and unmodified RNA oligos were mixture with DNA oligos to make up the RNA: DNA hybrid. HeLa cells transfected with siRNase H1 were re-transfected with Flag-RNase H1 ^{D209N} construct. The cells were extracted using NP40 buffer and cell lysates were subjected to biotin-pulldown assay by incubation of the cell lysates with the above made Biotin-R-Loops overnight at 4°C. Then the mixture was immunoprecipitated with Biotin-beads. After washing the beads with NP40 buffer for 3 times, the samples were then used for either mass spectrum or western blot analysis.

Proximity-dependent biotinylation identification assay (BioID)

HeLa cells were infected with BirA^{+}-ARID1A lentivirus for 48 h. After confluency, cells were either left untreated or treated with 10 Gy of IR and then subjected to incubate with 0.5 μg/mL biotin for 4 h and then harvested. After incubation, the chromatin extracts were isolated as above mentioned. Cell lysates were sonicated three times at 35% power using a cup sonicator following a cycle of 30 s on and 30 s off. Lysates were boiled for 10 min and vortexed every 3min. The lysates were then diluted in NETN lysis buffer (20 mM Tris at pH 8.0, 150 mM NaCl, 0.5% NP-40, 10% glycerol), precleared with protein A-conjugated magnetic beads, and then subjected to biotin pull-down with streptavidin-conjugated magnetic beads (M-280). Pull-downs were washed three times with NETN buffer. Pull-downs were then boiled in sample buffer and subjected to mass spectrometry analysis or Western blot.

Chromosome aberration assay

Chromosomal aberrations were analyzed by chromosome metaphase spreading.[78] First, cells were exposed to IR (3 Gy) and after recovery for 12 h, were pretreated with colchicine (0.4 μg/mL) for 3 h before harvesting. The collected cells were incubated in 0.8% sodium citrate for 15 min at 37°C and then fixed in a 3:1 methanol/acetic acid solution (three washes). The cells were resuspended in a small volume of fixative solution and dropped onto alcohol-cleaned slides and air dried. The cells were stained with DAPI before mounting and then images were captured under a confocal imaging system (Andor). More than 50 mitotic chromosomes were randomly analyzed.

Comet assay

A comet assay was performed as previously described.[79,80] Briefly, cells were either treated with etoposide (10 μM for 1 h) or irradiated with 3 Gy IR. After recovery, cells were harvested, counted, and resuspended in ice-cold PBS at a density of 5 × 10^5 cells/ml. The cells were then mixed with 37°C molten low-melting point agarose at a ratio of 1:10 (v/v) and the cell suspensions (50 μL) were transferred to prewarmed comet slides. The slides were kept at 4°C in the dark for 30 min and immersed in prechilled lysis buffer (2.5 M NaCl, 100 mM EDTA, 10 mM Tris·HCl, 1% N-lauroylsarcosine sodium, and 1% Triton X-100) for 1 h at 4°C followed by further

immersion in freshly prepared alkaline buffer for 30 min. Then, the slides were washed twice with 1× TBE buffer (90 mM Tris, 90 mM boric acid, and 3 mM EDTA) and subjected to TBE electrophoresis at 1.0 V/cm for 20 min. The slides were fixed in 100% ethanol for 5 min, air dried, and stained with 5 μg/mL propidium iodide at room temperature in the dark for 10 min. Images were captured under an Olympus BX51 fluorescence microscope (20× objective) and the tail moments of comets were quantified by ImageJ software with the OpenComet plugin.

Immunofluorescent staining

Cells were fixed with 4% paraformaldehyde and permeabilized with 0.5% Triton X-100. The cells were then incubated with blocking solution (3% BSA in PBS), followed by incubation overnight at 4°C with the primary antibody (γH2AX, 1:1,000; S9.6, 1:1,000; m6A, 1:3000; ARID1A,1:1000). The cells were then washed three times with cold PBS, and exposed to the appropriate Alexa Fluor 488-, 594-, or 647-conjugated secondary antibodies for 1 h at room temperature. After washing the cells three times with cold PBS, DAPI was used to stain nuclear DNA. Immunofluorescent images were captured under a Nikon confocal microscope.

In situ proximity ligation assay (PLA)

The R-Loop complexes PLA upon DNA damage were performed according to a described previously procedure.[81] Briefly, HeLa cells grown on confocal plates and treated with or without IR (5 Gy) were fixed with 4% (v/v) PFA in PBS for 15 min. After three washes in PBS, the cells were permeabilized with 0.5% Triton X-100 in PBS for 15 min followed by blocking with 3% (v/v) BSA in PBS for 1 h at room temperature. Cells were then double-stained with anti-S9.6 and anti-m6A primary antibodies for 2h at room temperature. PLA staining was then performed using a Duolink *In Situ* Red Starter Kit (mouse/rabbit) by which the cells were stained with Duolink *In Situ* PLA Probe Anti-Rabbit PLUS [affinity-purified donkey anti-rabbit IgG (H + L)] and Duolink *In Situ* PLA Probe Anti-Mouse MINUS [affinity-purified donkey anti-mouse IgG (H + L)] for 1 h at 37°C. After washing, the samples were incubated with the ligation-ligase solution for 30 min at 37°C to hybridize with the oligonucleotide-tagged probes. After two short wash steps, the cells were incubated with the amplification POL solution for 100 min at 37°C to amplify the hybridized oligonucleotides and ensure fluorescent labeling of the amplification products. The plates were then covered with Duolink *In Situ* Mounting Medium with DAPI. Imaging was performed under a Nikon confocal microscope and automated quantification of PLA foci was performed with ImageJ software.

Laser microirradiation-coupled live-cell imaging and IR

Laser micro-irradiation was performed as previously descried.[74,82] Briefly, cells were seeded into a glass-bottomed plate, and transfected with GFP-tagged plasmids for 24 h. The cells were then irradiated locally with a 365-nm pulsed nitrogen UV laser (16 Hz pulse, 41% laser output) generated by a MicroPoint Dye Laser System (Andor). This system was coupled directly to the epifluorescence path of the Nikon A1 confocal imaging system, and time-lapse images were captured every 10 s for 10 min. The signal intensity of the irradiation path from >30 cells was calculated using ImageJ software. For IR, the cells were exposed to an RS-2000pro X-ray irradiator (Rad Source Technologies) at a dose rate of 1.67 Gy/min.

S9.6 DRIP and m6A DIP

The S9.6 DRIP and m6A DIP were performed following a previous reported protocol.[28] Briefly, genomic DNA was isolated from HeLa cells by SDS/Proteinase K treatment at 37°C followed by incubation with 100 μg/mL RNase A/T1 for 30 min in lysis buffer, phenol-chloroform extraction and ethanol precipitation. gDNA of the control samples was treated with 10 U of RNase H (NEB, no. M0297S) in 1× RNase H buffer overnight at 37°C before immunoprecipitation. gDNA (10 μg) was used for immunoprecipitation. S9.6 DRIP was carried out using S9.6 antibody and anti-mouse magnetic Dynabeads. m6A DIP was performed using anti-m6A rabbit polyclonal antibody and magnetic anti-rabbit Dynabeads. The corresponding primary IgG-only and secondary IgG-only (Dynabeads-only) DRIP reactions were used in control immunoprecipitations. For the two-round (S9.6 DRIP followed by m6A DIP) DRIP/DIP, approximately 500 ng of the nucleic acids recovered from multiple DRIP reactions, performed in parallel, was used for m6A DIP followed by qPCR analysis.

Isolation of chromatin fractionation RNA

Chromatin associated RNA were isolated as described previously.[83] Briefly, the cells were treated as indicated and harvested for nuclear fraction isolation. The isolated nuclei were resuspended in 250 μL glycerol buffer, and then add the same volume of Urea buffer immediately. The mixture was incubated in ice for 2 min, followed by centrifuge the lysate at 13,000 g for 5 min, the pellet was briefly rinsed with PBS-EDTA solution, and then extracted with Trizol reagent and quantified by nanodrop.

Dot blots analysis

For the dot-blot analysis of R-Loops, the above-mentioned extracted genomic DNA was spotted onto Hybond N^+ membranes (GE Healthcare) and subjected to dot blotting with the anti-S9.6 antibody; For the m6A analysis, the above extracted chromatin-associated RNA was used as samples and spotted onto the membrane and subjected to dot-blot analysis using m6A antibody.

Microscale thermophoresis (MST) assay

Microscale thermophoresis was employed to study the interaction of RNase H1 with modified or unmodified RNA and the RNA: DNA hybrid synthetic substrates used in EMSA experiments. MST experiments were performed on a NanoTemper Monolith NT.115 with

fluorescence filters (NanoTemper Technologies GmbH, Munich, Germany). The His-RNase H1^{D209N} was bacterially-purified from the *E. coli*, and the different R-Loops were made up *in vitro* after oligos synthesized. Samples were prepared in the different buffers listed in the MST buffer section and loaded into standard/premium treated capillaries. Measurements were performed at 22°C using 20% MST power with laser off/on times of 5 s and 30 s, respectively, and 60% MST power with laser off/on times of 5 s and 20 s. All experiments were repeated three times for each measurement. Data analyses were performed using the NanoTemper analysis software. The Kd constants between the His-RNase H1^{D209N} and R-Loops were calculated using the saturation binding curve at equilibrium.

Chromatin immunoprecipitation (ChIP) and qPCR analysis

ChIP experiments were performed according to a described previously procedure.[84] Briefly, cells were crosslinked with 1.42% formaldehyde for 15 min at room temperature and quenched by the addition of glycine to a final concentration of 125 mM for 5 min. The fixed cells were washed twice with cold PBS and pelleted after scraping. The cell pellet was resuspended in IP buffer [150 mM NaCl, 50 mM Tris-HCl (pH 7.5), 5 mM EDTA, 0.5% NP-40, 1% Triton X-100] containing protease inhibitors and fragmented by sonication. For immunoprecipitation, the diluted chromatin was incubated with control or specific antibodies immobilized on Protein A/G Sepharose beads for 12 h at 4°C with constant rotation. The beads were washed five times with IP buffer and mixed with 100 μL 10% chelex (BioRad). The samples were boiled for 10 min and centrifuged for 1 min at 4°C, and the supernatants were transferred to new tubes. The pellets were washed again with 120 μL MilliQ water, mixed by vertexing for 10 s, and centrifuged to pellet the beads. The supernatants were combined and used as the template for follow-up qPCR analysis. PCR analysis was performed on a qTOWER3G touch Real-Time PCR Detection System (Analytik Jena AG) using SYBR Green Supermix (Vazyme, China) according to the manufacturer's instructions. All samples were analyzed in duplicate. The primers used for qPCR analysis are listed in key resources table.

TA colon-based deletion assay

AsiSI-U2OS cells were transfected with siNC and siARID1A using UltraFection 3.0 reagent for 2 days. Then, 4-OHT (500 nM) was added to cells to induce DSBs for 4 h, after which, the 4-OHT was removed and the cells were cultured for a further 2 days. Genomic DNA was extracted and used as the template for PCR as demonstrated in the diagram, and the PCR products were purified and cloned into a TA-vector. After LacZ selection, the PCR-amplified inserted products were analyzed by sequencing using the *RBMXL1* forward primer to determine the deletion size.

Flow cytometry

EJ5-GFP or DR-GFP U2OS cells were seeded in 6-well plates, treated as indicated and then infected with an I-SceI lentivirus. After 48 h, the cells were trypsinized and the percentage of GFP-positive cells was determined on a BD flow cytometer. The percentage of GFP-positive cells, which indicated the HR-mediated or NHEJ-mediated DSB repair efficiency, was determined.

Colony-formation assay

After 2 h of irradiation treatment, HeLa cells were seeded into a 6-well plate at a density of 500 cells/well and cultured for 2 weeks under normal conditions. The cells were then stained with crystal violet, and the number of colonies with >50 cells was counted.

Patient specimens treatment

The samples were thawed from liquid nitrogen and protein samples were isolated with RIPA lysis buffer. The extracts were centrifuged at 14,000 × g for 30 min and the supernatant was collected for further analysis. The concentration of each sample was quantified and equal amount of proteins were then subjected to western/dot blotting analysis using indicated antibodies.

Kaplan–Meier survival analysis

For each patient, Kaplan-Meier analysis was conducted to evaluate correlations of survival with ARID1A expression. A log rank test was applied to compare the survival distribution of patients with relatively high ARID1A expression and those with relatively low expression based on the lower quantile of all acquired expression data of various cancer patients who received chemotherapy using Kaplan-Meier Plotter database (https://kmplot.com/analysis/).

QUANTIFICATION AND STATISTICAL ANALYSIS

All data are presented as the means ± SD or means ± SEM as mentioned in the Figure legends. All experimental data were analyzed using GraphPad Prism 8. Significant differences between groups were evaluated by two-tailed, unpaired Student's *t*-tests, and differences were considered statistically significant at $^{*}p < 0.05$, $^{**}p < 0.01$, and $^{***}p < 0.001$. At least three independent replicates were performed in all experiments.

Cell Reports, Volume *43*

Supplemental information

The ARID1A-METTL3-m6A axis ensures effective RNase H1-mediated resolution of R-loops and genome stability

Jun Zhang, Feng Chen, Ming Tang, Wenchao Xu, Yuan Tian, Zhichao Liu, Yuxin Shu, Hui Yang, Qian Zhu, Xiaopeng Lu, Bin Peng, Xiangyu Liu, Xingzhi Xu, Monika Gullerova, and Wei-Guo Zhu

Supplemental Figures and Legends

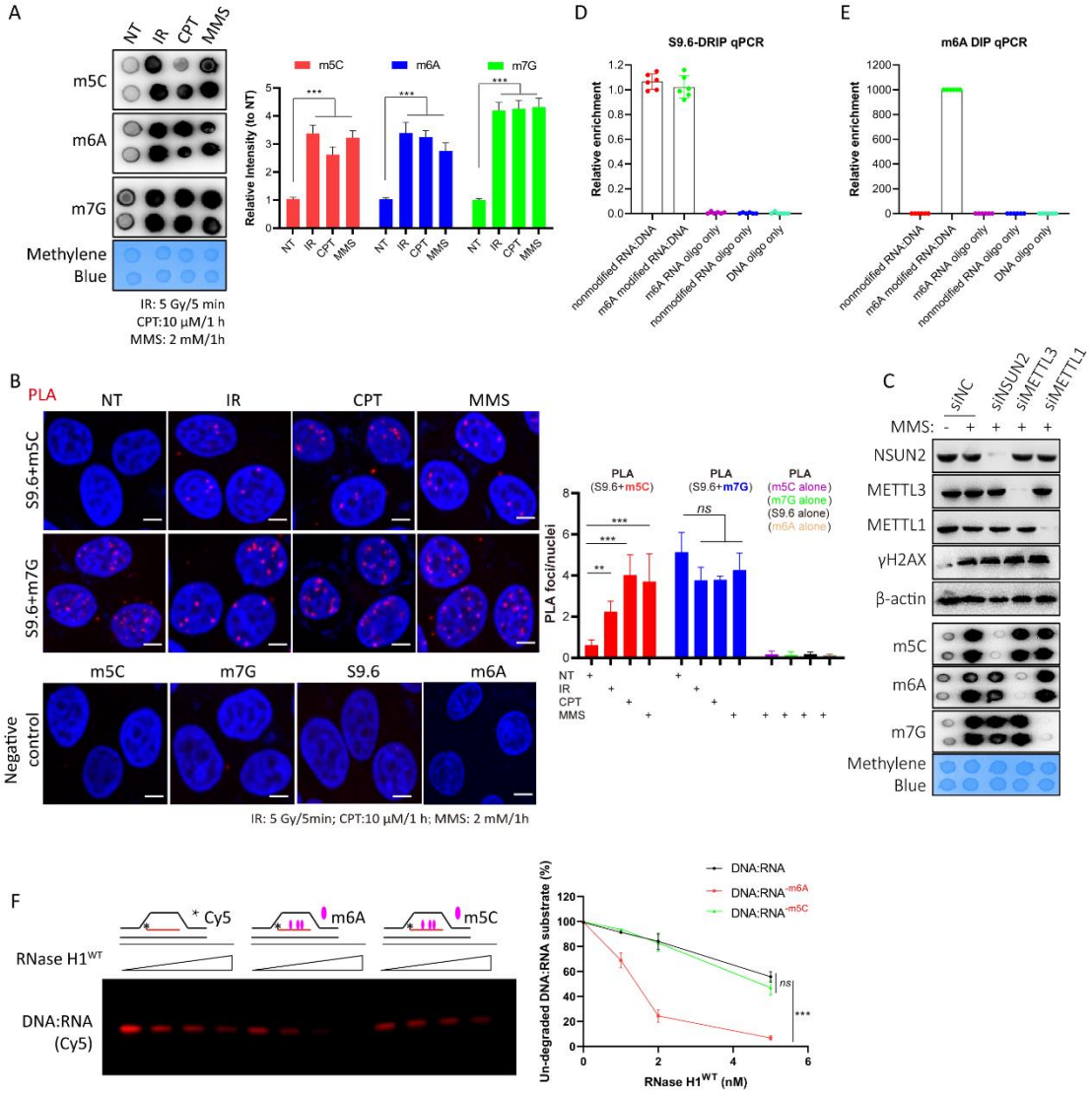

Figure S1, RNase H1 prefers to bind with m6A-modified R-Loop and catalyzes R-Loop resolution.

(A) Dot blot analysis of RNA methylation levels in HeLa cells after DNA damage stimulation. Cells were exposed to IR (5 Gy/5 min), CPT (10 μM for 1 h) and MMS (2 mM for 1 h). The cell lysates were subjected to dot blot analysis using specific antibodies. Methylene blue staining was used as a loading control. The relative intensity of each dot was quantified using Image J. The data represent the means ± SD. ***p< 0.001.

(B) *In situ* PLA of the interaction between S9.6 and m5C or m7G in HeLa cells treated with different DNA damaging-agents. The PLA foci was observed after staining with specific antibodies. Image shows an example of the *in situ* interaction between S9.6 and m6A visualized as red fluorescent dots (left) and quantification (n>30 cell per group) of PLA dots per nucleus (right). The data represent the means ± SEM. **p< 0.01; ***p< 0.001. Scale bar: 10 μM.

(C) Validation of the specificity of RNA methylation antibodies by knockdown of their corresponded methyltransferases. HeLa cells were transfected with the indicated siRNAs and followed by treatment with 2 mM MMS for 1 hour. Cells were then lysated and analyzed using the indicated antibodies.

(D-E) The *in vitro* R-Loop make-up efficiency was analyzed by S9.6-DRIP-qPCR and m6A-DIP-qPCR assay.

(F) The stability of un-modified or methylated-R-Loops was measured by Native-PAGE. The Cy5-labelled R-Loop, R-Loop^{m5C} and R-Loop^{m6A} substrates were incubated with increasing doses of RNase H1^{WT} (from 0 to 5 nM) *in vitro* for the 10 mins. The products were subjected to Native-PAGE, and the captured images were analyzed using a Fluorescence Imaging System. Image represents one of the three independent experiments. ***$p< 0.001$; *ns*, no significance.

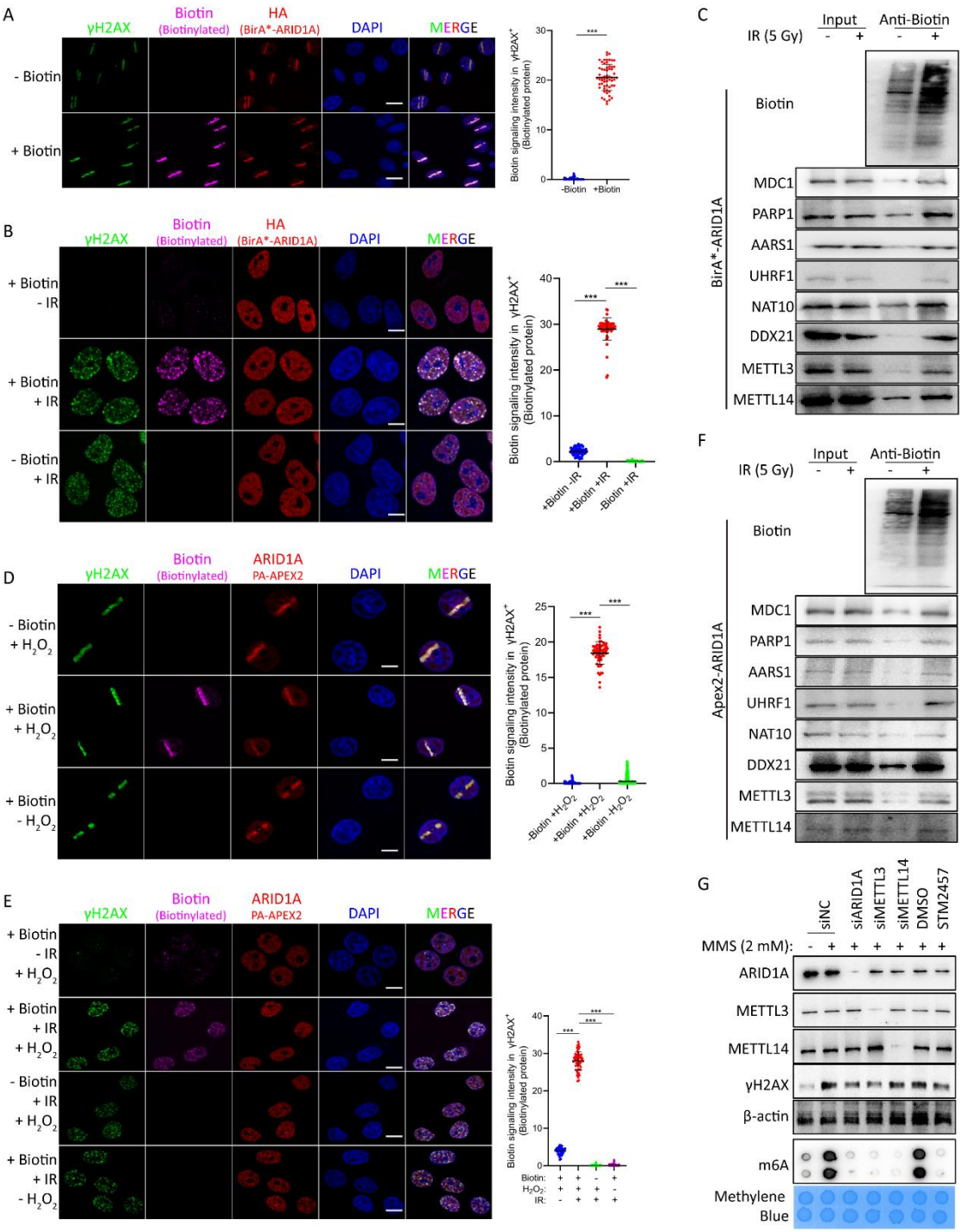

Figure S2, ARID1A facilities damage-induced R-Loop m6A modification on DSB-flanking chromatin in response to DNA damage.

(A-B) DNA damaged was induced in HeLa cells stably expressing BirA*-ARID1A by either microirradiation (A) or IR (5 Gy) (B). The cells were left to recover for 4 h in the presence or absence of exogenous biotin, and subjected to immunofluorescence to analyze colocalization of HA (BirA*-ARID1A) and biotin at sites of DNA damage. The fluorescent intensity of Biotin at DSB site was quantified with Image J. Image shows an example of the indicated antibodies staining, the

statistical quantification (n>30 cells for each group) were performed from three independent experiments. The data represent the means ± SEM. ***$p< 0.001$. Scale bar: 10 μM.

(C) BirA*-ARID1A expressing cells were incubated with biotin, treated or untreated with 5 Gy of IR, and then left to recover for 4 h. Cells were lysated and subjected to pulldown with streptavidin-conjugated beads. The indicated proteins in input extracts and IPs were analyzed by western blotting using the indicated antibodies.

(D-E) Localized protein biotinylation at DNA damage sites were identified using an APEX2-ARID1A labeling system. DNA damage was induced in HeLa cells by either microirradiation (D) or IR (5 Gy) (E). The cells were left to recover for 4 h in the presence or absence of exogenous biotin and subjected to immunofluorescence to analyze colocalization of ARID1A and biotin at sites of DNA damage. The fluorescent intensity of biotin at DSB site was quantified with Image J. Image shows an example of the indicated antibodies staining, the statistical quantification (n>30 cells for each group) were performed from three independent experiments. The data represent the means ± SEM. **$p< 0.01$; ***$p< 0.001$. Scale bar: 10 μM.

(F) APEX2-ARID1A-labeled proteins were extracted and subjected to pulldown with streptavidin-conjugated beads. The indicated proteins in the input extracts and IPs were analyzed by western blotting using the indicated antibodies.

(G) Validation of the knockdown efficiency of the indicated factors using western blot. HeLa cells were transfected with the indicated siRNAs and followed by treatment with 2 mM MMS. Cells were then lysated and subjected to western blot analysis using the indicated antibodies.

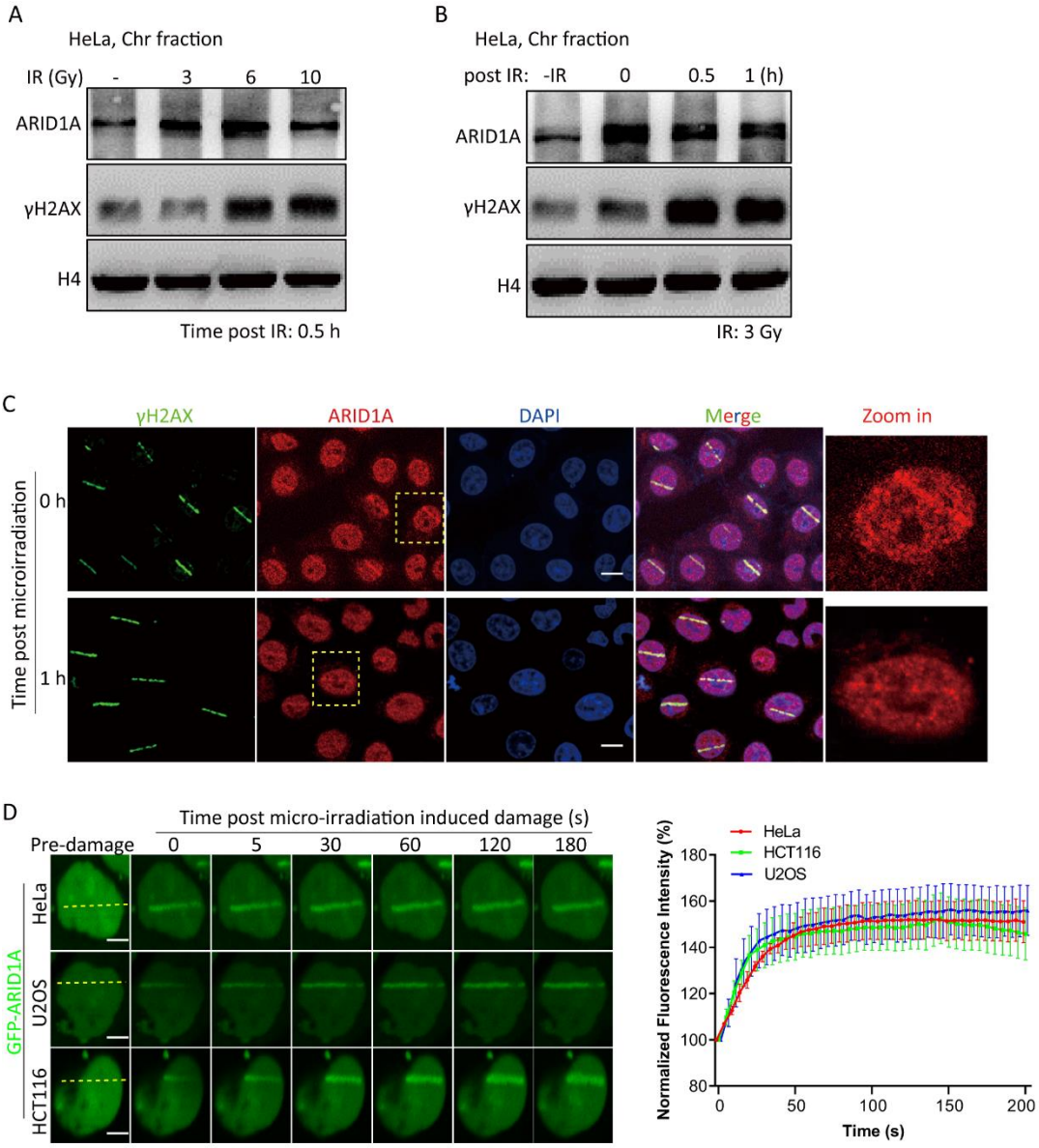

Figure S3, Chromatin-enriched ARID1A recognizes R-loops and facilities R-loop resolution at DSBs.

(A-B) Western blot showing specific antibody signals in the chromatin fractions from HeLa cells treated with different doses of IR (0.5 h) (A) or different time releases post 3 Gy IR (B).

(C) Immunofluorescence staining showing the ARID1A and γH2AX signal at laser microirradiatiation-induced DSBs in HeLa cells. The nuclei were counterstained with DAPI. Scale bar: 10 μM.

(D) The dynamics of ARID1A accumulation at DNA damage sites was monitored by laser microirradiation-coupled live-cell imaging of HeLa, HCT116 and U2OS cancer cell lines. GFP-ARID1A accumulation intensity at DSBs was quantified by Image J (n >30). Scale bar: 20 μM.

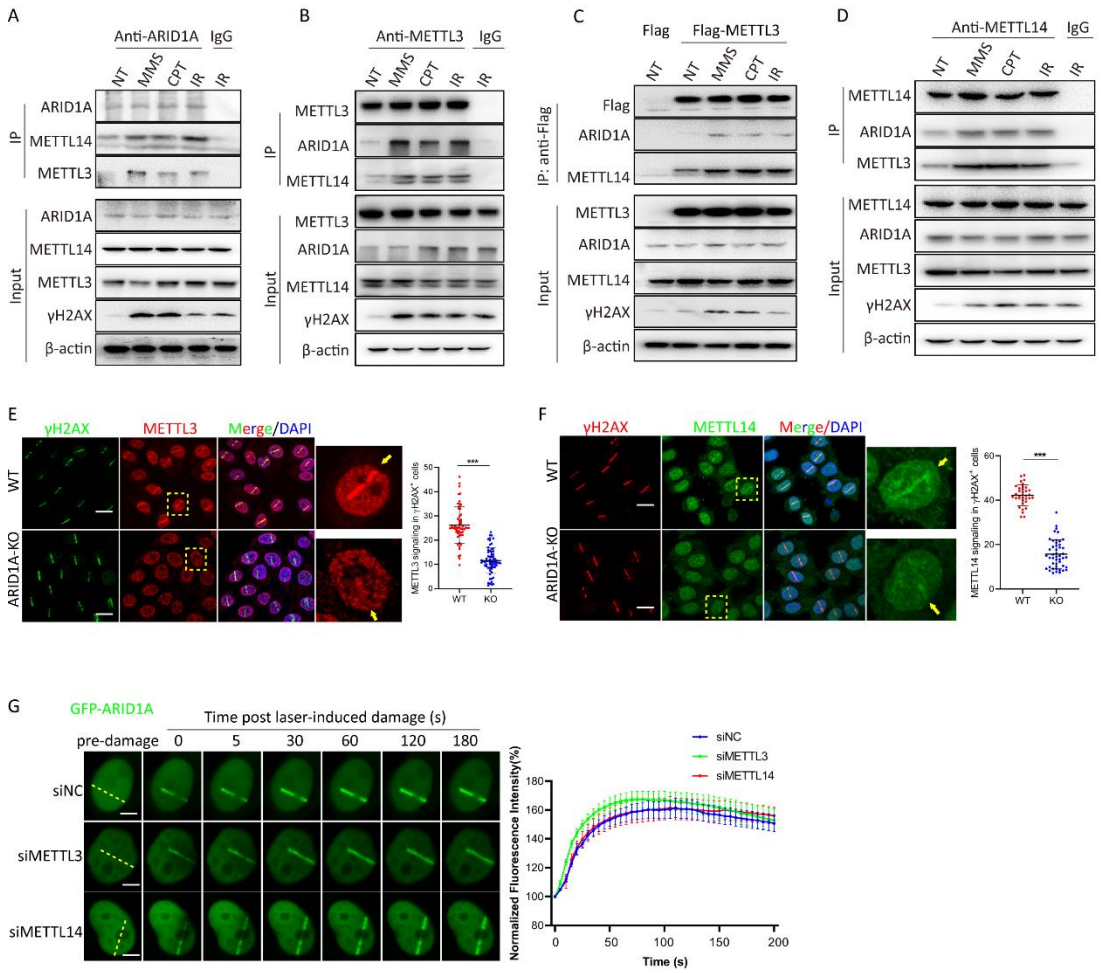

Figure S4, ARID1A recruits METTL3/14 to R-Loop and facilities R-Loop RNA m6A modification

(A-B) Immunoprecipitation analysis of the endogenous interaction between ARID1A and METTL3 and METTL14. HeLa cells were treated with IR (5 Gy/5 min), CPT (10 μM for 1 h) or MMS (2 mM for 1 h), respectively, before the cell lysates underwent co-immunoprecipitation using anti-ARID1A (A) or Anti-METTL3 (B) antibodies. The immunoprecipitated products were analyzed by western blotting with the indicated antibodies.

(C-D) Immunoprecipitation analysis of the interaction between ARID1A and METTL3 and METTL14. HeLa cells overexpressing either Flag-METTL3 (A) or Flag-METTL14 (B) were treated with IR (5 Gy/5 min), CPT (10 μM for 1 h) and MMS (2 mM for 1 h), respectively. The cell lysates were subjected to co-immunoprecipitation using an anti-Flag antibody, and the immunoprecipitated products were analyzed by western blotting using the indicated antibodies.

(E-F) Immunofluorescence staining showing METTL3 and METTL14 recruitment at γH2AX signals at microirradiatiation-induced DSBs in HeLa and HeLa-ARID1A-deficient cells. The nuclei were counterstained with DAPI. Image shows an example of the indicated antibodies staining, the statistical quantification (n>30 cells for each group) were performed from three independent experiments. The data represent the means ± SEM. ***p< 0.001. Scale bar: 10 μM.

(G) Dynamics of GFP-ARID1A accumulation at DNA damage sites in siNC, siMETTL3 and siMETTL14 transfected cells monitored by laser micro-irradiation-coupled live-cell imaging. The fluorescent intensity at DSB site was quantified with Image J. Scale bar: 20 μM.

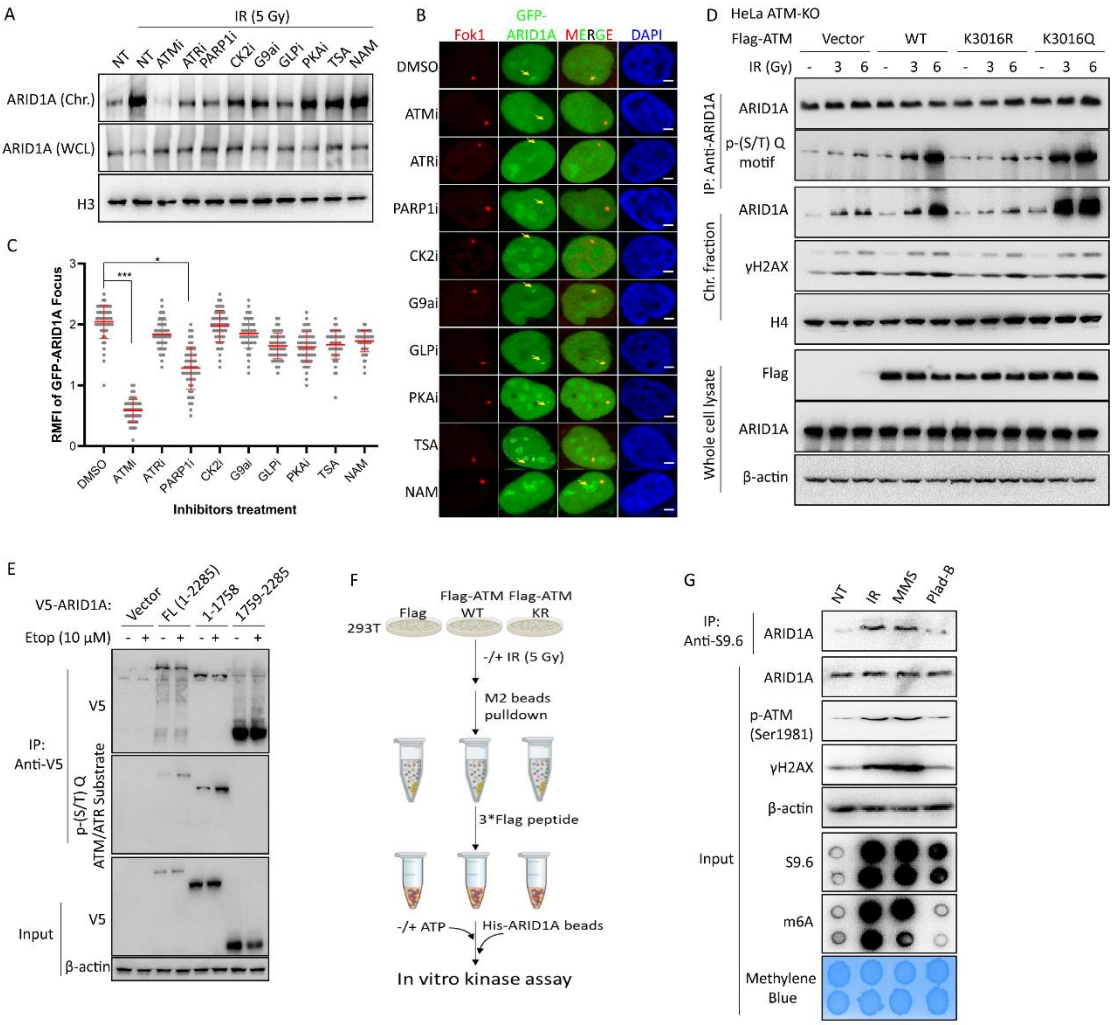

Figure S5, ATM-dependent recruitment of ARID1A to DSB site is required for R-Loop resolution.

(A) Western blot showing specific ARID1A signals in the chromatin and whole cell lysate fractions from HeLa cells treated with different kinase/enzyme inhibitors, as indicated.

(B) Small molecule inhibitor screen. U_2OS-265 DSB reporter cells were transfected with GFP-ARID1A. Then, the cells were preincubated with the indicated inhibitors for 1 h, followed by the introduction of site-specific DSBs. Representative images after DNA damage are shown. Image shows an example of the indicated antibodies staining. Scale bar: 20 μM.

(C) The GFP-ARID1A relative mean fluorescence intensity was quantified and calculated with Image J software. The statistical quantification (n>30 cells for each group) were performed from three independent experiments. The data represent the means ± SEM. *p< 0.05; ***p< 0.001.

(D) HeLa-ATM-KO cells overexpressing WT, K3016R or K3016Q constructs were subjected to the indicated doses of IR and then released for 30 mins. The cells were then either extracted for IP assay using anti-ARID1A antibody, or cellular fractions were isolated for western blotting using the indicated antibodies.

(E-F) HeLa cells overexpressing different ARIDA fragments were treated with Etoposide (10 μM for 1 h). Then, the cells were lysed and subjected to immunoprecipitation using an anti-V5 antibody. The phosphorylation status of ARID1A was analyzed using a p-S/TQ antibody.

(G) HeLa cells were treated as indicated, the cells were harvested and lysated. Then cell lysates were introduced to analysis using the indicated antibodies.

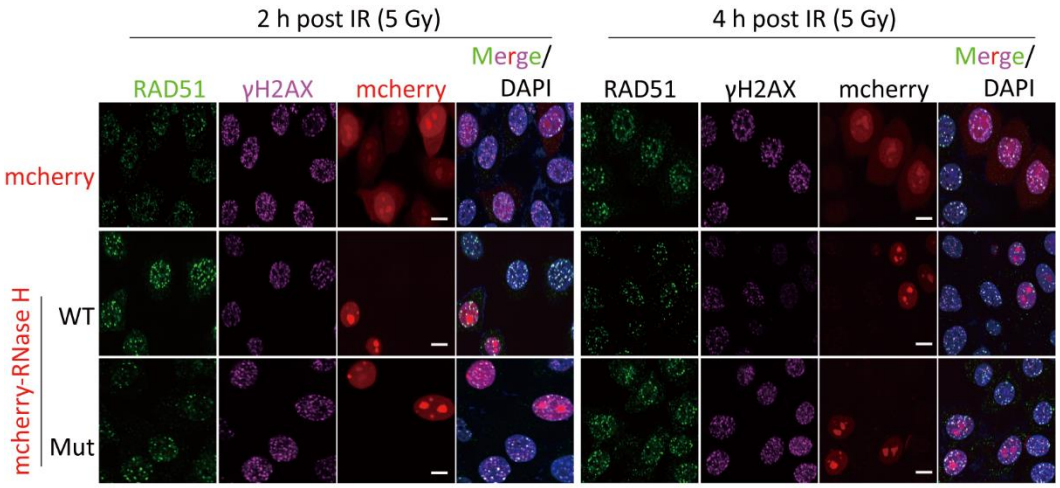

Figure S6, ARID1A mediated R-loop resolution facilities end resection and DNA damage repair.

(A) IF staining showing γH2AX and RAD51 foci formation kinetics and disappearance from mCherry-RNase H1 WT and enzymatic-dead mutant expressing HeLa cells exposed to 5 Gy IR. Representative γH2AX and RAD51 foci are shown. Scale bar: 10 μM.

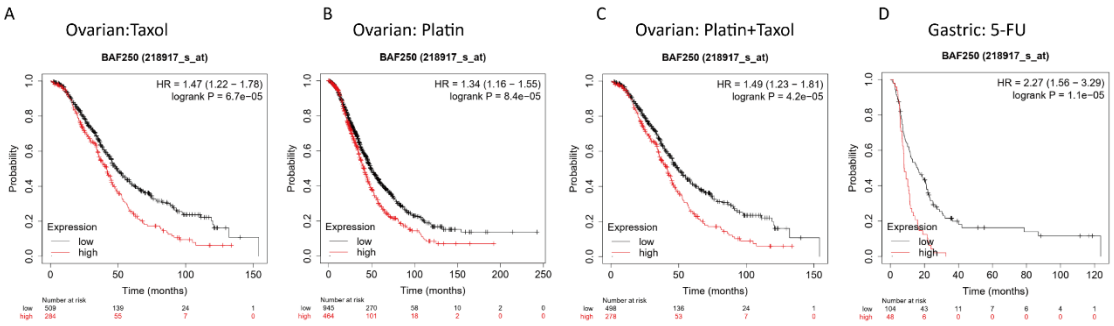

Figure S7, ARID1A is a critical mediator of genome stability maintenance and cellular resistance to DNA-damaging treatment.

Kaplan–Meier analysis of ARID1A expression and its correlation with overall survival in patients with ovarian cancer treated with Taxol (A), Platin (B) or Taxol plus platin (C), or gastric cancer treated with 5-FU (D). Analysis was performed using the Kaplan-Meier Plotter database (https://kmplot.com/analysis/). The hazard ratio and 95% confidence interval values are shown. In each case, the *P*-values were obtained by log-rank test.